Journal of Elasticity
https://doi.org/10.1007/s10659-024-10100-w

RESEARCH

Deformation of a Planar Ferromagnetic Elastic Ribbon

G. R. Krishna Chand Avatar[1] · **Vivekanand Dabade**[1]

Received: 22 April 2024 / Accepted: 23 November 2024
© The Author(s), under exclusive licence to Springer Nature B.V. 2024

Abstract
In this paper we explore the influence of magnetisation on the deformation of planar ferromagnetic elastic ribbons. We begin the investigation by deriving the leading-order magnetic energy associated with a curved planar ferromagnetic elastic ribbon. The sum of the magnetic and the elastic energy is the total energy of the ribbon. We derive the equilibrium equations by taking the first variation of the total energy. We then systematically determine and analyse solutions to these equilibrium equations under various canonical boundary conditions. We also determine the stability of the equilibrium solutions. Comparing our findings with the well-studied Euler's elastica provides insights into the magnetic effects on the deformation behaviour of elastic ribbons. Our analysis contributes to a deeper understanding of the interplay between magnetisation and the mechanical response of planar ferromagnetic structures, and offers valuable insights for both theoretical and practical applications.

Keywords Magnetoelastic slender structures · Soft ferromagnets · Hard ferromagnets · Ribbons · Elastica

Mathematics Subject Classification 74B20 · 74F15 · 74G60

1 Introduction

Ferromagnetic ribbons and slender structures exhibit complex coupling between magnetism and deformation or elasticity and they offer the potential to achieve substantial deformations using remote external magnetic fields. Novel deformations, unachievable in purely elastic slender structures, find interesting applications in advanced actuators and sensors fabricated from ferromagnetic slender structures [16, 22, 23]. For instance, the concept of a stowed preloaded structure, which can transition into novel configurations upon the application of a small external magnetic field, holds promise for diverse applications in deployable structures. In this paper, we employ concepts drawn from the theory of micromagnetics and Euler's elastica to construct a model aimed at analysing the planar deformation of ferromagnetic ribbons.

Motivated by the aforementioned applications and prospects of ferromagnetic slender structures, our study focuses on analysing the interplay between magnetism and deformation in ferromagnetic ribbons. We adopt a variational approach for this problem and begin

✉ V. Dabade
dabade@iisc.ac.in

[1] Department of Aerospace Engineering, Indian Institute of Science, Bengaluru 560012, India

our analysis by deriving the total energy of the ferromagnetic ribbon undergoing planar deformation. The total energy of a ferromagnetic slender ribbon is given by the sum of the elastic energy, magnetic energy of the ribbon and energy due to a mechanical loading device. The elastic energy is equal to the bending energy, as we shall assume that the ribbon is inextensible. The rationale for selecting this particular model for the elastic energy of the ferromagnetic planar ribbon is justified in Sect. 2.1. The magnetic energy is formulated based on the theory of micromagnetics.

Micromagnetics is a continuum theory for magnetism that has proven to be a robust model capable of explaining and predicting the diverse array of magnetic domain structures observed in ferromagnetic materials [3, 8]. The magnetisation vector $\boldsymbol{m}(\boldsymbol{x})$ is the primary variable in the micromagnetics functional. The magnetisation vector $\boldsymbol{m}(\boldsymbol{x})$ is a unit-normed vector supported on a ferromagnetic body. The micromagnetics functional is expressed as the sum of exchange energy, magnetocrystalline anisotropy energy, magnetostatic (abbreviated as demag.) energy, and Zeeman energy, as detailed in [8] and [5]. The exchange energy is characterized by a material constant known as the exchange constant, denoted as A. Similarly, the anisotropy energy is characterized by a material constant known as the anisotropy constant, denoted as K_a. Both demag. and Zeeman energy are characterized by a material constant known as the magnetostatic energy density constant, denoted as K_d. Thus, the constants A, K_a, and K_d describe the ferromagnet according to the micromagnetics functional. We refer the reader to Sect. 2.2 for a concise discussion on the micromagnetics functional.

Ferromagnets are commonly categorised into soft and hard ferromagnets, depending on the relative magnitudes of K_a and K_d. In soft ferromagnets $K_d \gg K_a$, while in hard ferromagnets $K_a \gg K_d$. In this study, we investigate both soft and hard ferromagnetic ribbons. In soft ferromagnetic ribbons, the demag. energy influences the deformation of the ribbon. The demag. energy, strongly depends on the shape of the body and is computed by solving Maxwell's equations of magnetostatics. Due to the non-local nature of the demag. energy, calculating it is computationally expensive and challenging for general three-dimensional bodies, as it requires the calculation of the magnetic field in the entire space surrounding the body. However, for slender structures, the leading order demag. energy is local in nature and assumes simpler forms, offering an opportunity to explore these problems (semi-) analytically. In hard ferromagnetic ribbons, the Zeeman energy influences the deformation of the ribbon. In such materials, magnetization remains fixed along specific preferred directions known as the easy axis of the material. The Zeeman energy seeks to orient the body such that these preferred directions are aligned with the external magnetic field. Hence, our analysis focuses on the deformation of a slender body resulting from the interplay of demag. energy and Zeeman energy along with elastic energy.

The demagnetization (and Zeeman) energy scales very differently compared to the elastic energy in bulk versus slender ferromagnets. This disparity in scaling leads to significantly larger displacements in slender ferromagnetic structures compared to bulk ferromagnets under an identical external magnetic field. In bulk ferromagnetic materials, the elastic energy density scales as Young's modulus E ($\sim 10^{11} J/m^3$), whereas the demag. energy scales as K_d ($\sim 10^5 J/m^3$). Here, K_d and E represent the magnetostatic energy constant and Young's modulus of the material, respectively, with both being material parameters. Bulk ferromagnetic solids (Iron, Nickel, Galfenol etc.) are known to deform when magnetised. This phenomenon is known as Joule magnetostriction. However, even under strong external magnetic fields, magnetostriction strains are small, typically on the order of 10^{-5}. Our work does not consider Joule magnetostriction; rather, we are primarily interested in understanding the deformation in slender ferromagnetic structures due to the effects of demag. energy and Zeeman energy. The elastic energy and magnetic energy are comparable in slender ferromagnetic structures, even though the elastic energy density is typically much greater than

the magnetic energy density in bulk ferromagnetic materials. Hence, we can obtain large displacements in ferromagnetic slender structures while the strains in bulk ferromagnetic solids due to Joule magnetostriction are very small.

In slender ferromagnetic structures, the interplay between elastic and magnetic energy becomes significant. The dissimilar scaling of these energies with respect to the aspect ratio allows their magnitudes to become comparable. The leading-order demag. energy of a slender ferromagnetic ribbon scales as $\mathcal{O}(K_d atl)$, and the elastic energy scales as $\mathcal{O}\left(\frac{EI}{2l}\right)$. Here, thickness, width, and length of the ferromagnetic ribbon are denoted as t, a, and l, respectively, and $I = \frac{at^3}{12}$, is the area moment of inertia, see Fig. 1. Hence, ferromagnetic slender structures offer an opportunity to tune the aspect ratio, allowing the interaction between demag. energy and elastic energy. A balance of these energies implies that our analysis is valid for ribbons with an aspect ratio of $\mathcal{O}\left(\sqrt{\frac{E}{24K_d}}\right)$.

In this study, we consider a ferromagnetic planar ribbon composed of a ferromagnetic material such as Iron or Nickel. Our focus lies in investigating the influence of magnetization on ribbon deformation as the applied load varies quasi-statically. In particular, we shall study the two following cases:

- *Case 1. (Soft ferromagnet)*: Magnetisation vector $\boldsymbol{m}(\boldsymbol{x})$ is spatially constant and does not change with deformation. This case characterises soft ferromagnetic materials such as Permalloy, with an external magnetic field large enough to saturate the magnetisation uniformly throughout the deformed planar ribbon.
- *Case 2. (Hard ferromagnet)*: Magnetisation vector $\boldsymbol{m}(\boldsymbol{x})$ makes a constant angle with respect to the tangent of the deformed planar curve. Here, the tangent vector, and hence the magnetisation vector vary spatially as the slender body undergoes deformation. This case characterises hard ferromagnetic materials such as Neodymium or Samarium-Cobalt.

To recapitulate, the total energy of a one-dimensional ferromagnetic ribbon is the summation of its elastic energy, exchange energy, anisotropy energy, demag. energy, Zeeman energy, and mechanical loading device energy. Calculating the elastic energy, anisotropy energy, Zeeman energy, and mechanical loading device energy are straightforward. However, determining the demag. and exchange energies for a curved ferromagnetic ribbon requires computations to be performed within the curvilinear local material frame. We obtain the leading order demag. energy for a curved ferromagnetic ribbon by employing a local material frame aligned with the tangent line of the deformed curve. Working in the deformed configuration alleviates the need to define a pull-back for the magnetisation vector $\boldsymbol{m}(\boldsymbol{x})$ and solving the Maxwell's equations of magnetostatics in the reference configuration. Various pullbacks for magnetisation are defined in the literature, posing challenges in the rational selection of the appropriate one, [13, 14]. The leading order demag. energy is local in nature and hence amenable for analysis. We also derive the exchange energy for our one-dimensional ferromagnetic ribbon. Our exchange energy matches with findings reported in the field of curvilinear micromagnetics [25, 29] to leading order. With the effective energy functional of the ribbon derived, we proceed to the next step of determining the energy-minimizing deformations as the external load is increased in a quasi-static manner.

We determine the deformed configuration by solving the equilibrium equations obtained by taking the first variation of the total energy. The equilibrium equations show that the magnetisation produces a body couple along the length of the curve that is dependent on the local orientation of the curve, in addition to the conventional terms originating from elastic energy, see Eqn. (24). The equilibrium equations are solved numerically for various canonical boundary conditions, using AUTO-07p, a standard software used in continuation and

bifurcation problems [9, 10]. Further, we also perform a stability analysis of our computed solutions. The stability analysis involves casting the second variation of the total energy as a Sturm-Liouville boundary value problem. The eigenvalues of this boundary value problem, as the load is varied continuously, are used to determine the stability of the deformed configurations.

We obtain the equilibrium path and the stability of the first few relevant modes, under quasi-static load control simulation. Our results provide us with a stable deformed state of the ferromagnetic ribbon, beginning from zero load and, in certain instances, a moderate tensile load, and extending to an arbitrarily large compressive load. The main findings from our analysis are as follows:

Case 1: Soft ferromagnetic ribbon:

- Critical buckling load is determined to be tensile under all canonical boundary conditions. Refer to Figs. 11, 12 and 13.
- Fixed-fixed boundary conditions reveal the emergence of novel stable curves on the mode-2 branch. In Fig. 12 (a), we highlight the segment of the mode-2 branch that corresponds to novel stable configurations, observed in a ferromagnetic ribbon but absent in Euler's elastica. A novel stable mode shape featuring two self-intersection points is shown in red in Fig. 12 (a), and additional illustrations can be found in Fig. 12 (b).

Case 2: Hard ferromagnetic ribbon:

- Introduction of magnetization alters the compressive buckling load compared to the elastica. See Figs. 14, 15 and 16.
- Comparing the deformed configuration of the hard ferromagnetic ribbon to Euler's elastica, no discernible difference in shape is observed, despite the presence of a change in the vertical reaction force at the supports. The expressions for the vertical reaction forces at the supports are provided in Equations (84) and (85).

Before proceeding to the main body of the paper, we compare and contextualize our work with the existing literature. Several researchers have studied the deformation of ferromagnetic ribbons under an external magnetic field, primarily focusing on cantilever configurations, that is, with fixed-free boundary conditions. Some of the foundational research related to deformation of planar ferromagnetic ribbons traces its origins back to the 1960s, where Moon et al. [18, 19] investigated the onset of buckling instabilities in a cantilevered beam-plate under magnetic loading [18, 19]. The distributed magnetic torque is dependent on θ. Here, θ represents the angle formed by the local tangent with respect to the horizontal, see Fig. 2. Our model recovers this limit for $\theta \ll 1$. Furthermore, the scaling for critical magnetic load, $B_c \sim \left(\frac{l}{t}\right)^2$ matches with our prediction (See Sect. 3.3 for detailed comparison). The buckling of slender ferromagnetic structures has also garnered attention in the recent past. Singh et al. [27] studied nonlinear elastic deformations in a vertically cantileverd Euler-Bernoulli beam with a permanent magnet attached to the free end. Their work explored both supercritical and subcritical bifurcation behaviors under the combined influence of a uniform magnetic field and a hard magnet. Gerbal et al. [11] investigated magnetoelastic buckling transition in ferromagnetic cantilevered rods. Similar to [11], Wang et al. [30] developed a mathematical model for hard magnetic cantilevered beam and determined critical load and the mode deformation under external magnetic fields varying in intensity and direction. We have recovered the equilibrium equation corresponding to the hard magnetisation distribution of a magnetically loaded cantilevered beam which matches with that derived in [11, 30]. Singh et al. [26] studied the occurrence of magnetically-induced instability in cantilever beams using small deflection assumptions. The main focus of these investigations

has been to determine the critical external magnetic field at which the cantilever buckles, while either maintaining a fixed external load or having no load applied. In contrast, our work has centered on maintaining a constant external magnetic field while quasi-statically varying the applied load.

1.1 Organisation of the Paper

The paper is organised as follows: In Sect. 2, we present the mathematical model for the ferromagnetic planar ribbon. Beginning with the geometry and kinematics, we then derive the total energy of a ferromagnetic planar ribbons. In Sect. 3, we obtain the total energy functionals for soft and hard ferromagnetic planar ribbons, and the corresponding equilibrium equations for various canonical boundary conditions. In Sect. 4, we describe the numerical continuation method employed for solving the equilibrium equations. Section 5, focuses on the stability analysis of the solutions to the equilibrium equations. Section 6 details the numerical solutions for various canonical loading scenarios. We comprehensively analyse the deformation behaviour and bifurcation patterns for various canonical loading scenarios. The end of Sect. 6 is devoted to a discussion in the limit as $\bar{K}_d$ approaches infinity. Here, $\bar{K}_d = \frac{K_d a t l^2}{EI}$ represents the ratio of the magnetostatic energy density to the elastic energy density of the ferromagnetic ribbon. We close our paper with the conclusions and remarks in Sect. 7.

2 One-Dimensional Model for a Ferromagnetic Ribbon

We begin with the kinematic description of ribbons. Ribbons are characterized by three disparate length scales – length (l), width (a), thickness (t) – such that $t \ll a \ll l$. Geometrically, ribbon is described in terms of a three-coordinate set – centerline arc length (s), lateral ($\tilde{a}$), transverse ($\tilde{t}$) coordinates. In the reference configuration, the ribbon is represented in standard basis of $(\boldsymbol{e}_1, \boldsymbol{e}_2, \boldsymbol{e}_3)$ as $\boldsymbol{x}_0(s, \tilde{a}, \tilde{t}) = s\boldsymbol{e}_3 + \tilde{a}\boldsymbol{e}_1 + \tilde{t}\boldsymbol{e}_2$. We assume that the centreline of the ribbon lies in the $\boldsymbol{e}_2 - \boldsymbol{e}_3$ plane without undergoing any twist in the deformed configuration. The centreline representation of the deformed planar ribbon is given by

$$\boldsymbol{x}(s, \tilde{a}, \tilde{t}) = \boldsymbol{r}(s) + \tilde{a}\boldsymbol{d}_1(s) + \tilde{t}\boldsymbol{d}_2(s). \tag{1}$$

Here, $\boldsymbol{r}(s)$ denotes the position vector of a material point on the centreline, $(\boldsymbol{d}_1(s), \boldsymbol{d}_2(s), \boldsymbol{d}_3(s))$ is the orthonormal material frame basis, and $s \in [0, l]$, $\tilde{a} \in [-a/2, a/2]$, $\tilde{t} \in [-t/2, t/2]$. The ribbon is uniform and is assumed to be inextensible and unshearable. The condition of inextensibility implies that $\frac{\mathrm{d}\boldsymbol{r}}{\mathrm{d}s} = \boldsymbol{d}_3(s)$. Due to the unshearability condition, the ribbon adheres to Kirchhoff's hypothesis, which states that normal sections to the centreline remain normal after deformation [2]. Furthermore, since the ribbon does not twist, we have $\boldsymbol{d}_1(s) = \boldsymbol{e}_1$. Now, the material basis vector $\boldsymbol{d}_2(s) = \boldsymbol{d}_3(s) \times \boldsymbol{e}_1$. Thus, $\boldsymbol{r}(s)$ is the only vector required to completely describe the kinematics of the rod. The material basis vectors evolve with arc length coordinate (s) as

$$\begin{aligned} \boldsymbol{d}_1'(s) &= 0, \\ \boldsymbol{d}_2'(s) &= \kappa^{(1)}\boldsymbol{d}_3(s) = \kappa\boldsymbol{d}_3(s), \\ \boldsymbol{d}_3'(s) &= -\kappa^{(1)}\boldsymbol{d}_2(s) = -\kappa\boldsymbol{d}_2(s). \end{aligned} \tag{2}$$

Here, $\kappa^{(1)} = \kappa(s)$ represents the material curvature associated with $\boldsymbol{d}_1(s) = \boldsymbol{e}_1$.

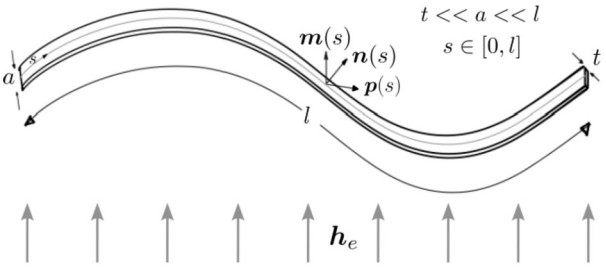


Fig. 1 Geometry of the ferromagnetic ribbon illustrating the representation of magnetisation vector $\boldsymbol{m}(s)$, easy axis $\boldsymbol{p}(s)$, and normal vector $\boldsymbol{n}(s) = \boldsymbol{d}_2(s)$

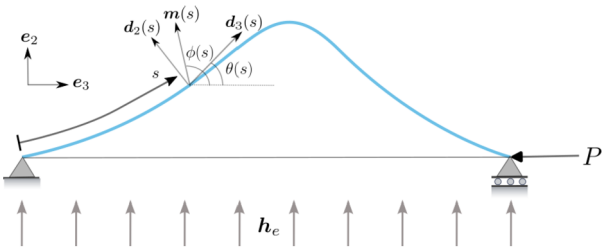


Fig. 2 Schematic setup of the ferromagnetic ribbon

The schematic of the centerline in the deformed configuration is shown in Fig. 2, and the coordinates of the centerline in $(\boldsymbol{e}_1, \boldsymbol{e}_2, \boldsymbol{e}_3)$ basis is given as follows:

$$x(s) = 0, \qquad y(s) = \int_0^s \sin\theta(t)\, dt, \qquad z(s) = \int_0^s \cos\theta(t)\, dt, \tag{3}$$

where s denotes arc length coordinate, $\theta(s)$ is the angle between $\boldsymbol{d}_3(s)$ and $\boldsymbol{e}_3$ basis vector at s. The tangent vector field $\boldsymbol{d}_3(s)$ (or $\boldsymbol{t}(s)$) is $\boldsymbol{d}_3(s) = (0, \sin\theta(s), \cos\theta(s))$ and so the normal vector field [21] is $\boldsymbol{n}(s) = \boldsymbol{d}_2(s) = \frac{\boldsymbol{t}'(s)}{\kappa(s)} = (0, \cos\theta(s), -\sin\theta(s))$. Note that the curvature $\kappa(s) = \theta'(s)$.

The magnetic variables involved in the description of the ferromagnetic ribbon are the magnetisation vector $\boldsymbol{m}(s)$ and the externally applied magnetic field $\boldsymbol{h}_e$. For both soft and hard ferromagnetic ribbons, we justify that the magnetization vector is solely determined by the centerline arc-length coordinate, denoted as s. The angle formed by the magnetization vector $\boldsymbol{m}(s)$ and the reference direction $\boldsymbol{e}_3$ is represented by $\phi(s)$, as depicted in Fig. 2. In this paper, we consider the external applied magnetic field in the transverse direction, represented by $\boldsymbol{h}_e = (0, h_e, 0)$, where h_e denotes the magnitude of the external magnetic field. We now proceed to formulate the mechanical and the magnetic energy of the ferromagnetic ribbon.

2.1 Mechanical Energy

The free energy functional of ferromagnetic ribbon is equal to the sum of its magnetic energy, elastic energy and the loading device energy. Given our assumption that the ribbon is made of an inextensible ferromagnetic material, the primary source of the elastic energy is the bending energy. We denote the sum of the bending energy and the loading device energy as $\mathcal{E}_{\text{elastica}}$ which is given as follows:

$$\mathcal{E}_{\text{elastica}} = \underbrace{\frac{1}{2}\int_0^l EI\kappa^2(s)ds}_{\text{Elastic (or bending) energy}} + \underbrace{P\left(l - \int_0^l \cos\theta(s)ds\right)}_{\text{Loading energy}}, \tag{4}$$

subject to the integral constraint

$$y(l) = \int_0^l \sin\theta(s)\, ds = 0. \tag{5}$$

This constraint implies that the y-coordinate of the centerline at $s = l$ is zero. Here, $\kappa(s) = \frac{\mathrm{d}\theta(s)}{\mathrm{d}s}$ represents the bending curvature, E denotes Young's modulus, $I = \frac{at^3}{12}$ is the area moment of inertia (with EI as the bending stiffness of the cross section), and P is the horizontally applied dead load.

We use Kirchhoff rod theory to describe the deformation of our ferromagnetic ribbon. The Kirchhoff rod theory serves as an appropriate framework for describing the deformation of ribbons, when the dimensionless parameter $\bar{\kappa} \sim \frac{\kappa a^2}{t} \ll 1$, as discussed in [1]. For a ferromagnetic ribbon that is considered in our work, we can estimate $\bar{\kappa}$ as follows: $\bar{\kappa} = \frac{\kappa a^2}{t} \ll \frac{\kappa_c a^2}{t} = \left(\frac{a}{t}\right)^2 \sqrt{\frac{K_d}{E}}$. Here, κ_c is the maximum curvature of the ferromagnetic ribbon and is estimated as $\kappa_c \sim \mathcal{O}\left(\frac{1}{t}\sqrt{\frac{K_d}{E}}\right)$, see Sect. 6.4 for the derivation of κ_c. For a typical ferromagnetic material, $K_d \sim \mathcal{O}(10^5\, J/m^3)$, and $E \sim \mathcal{O}(10^{11}\, J/m^3)$ implying that $\frac{K_d}{E} \sim \mathcal{O}(10^{-6})$ and thus $\bar{\kappa} \ll 1$ for $\frac{a}{t} \sim \mathcal{O}(10^1)$. Therefore, the Kirchhoff rod model serves well for a typical ferromagnetic ribbon of aspect ratio 10 or smaller.

2.2 Magnetic Energy

We now proceed to write down the magnetic energy of the ribbon. We employ the theoretical framework of micromagnetics to formulate the magnetic energy associated with a ferromagnetic ribbon. Recall that the magnetisation vector ($\boldsymbol{m}(\boldsymbol{x})$), is the primary variable in the micromagnetics functional. The magnetisation vector $\boldsymbol{m}(\boldsymbol{x})$ is supported on Ω and $|\boldsymbol{m}(\boldsymbol{x})| = 1$, $\boldsymbol{x} \in \Omega$. In our analysis, Ω represents the deformed planar ferromagnetic ribbon. We now examine the various terms of the micromagnetic functional when applied to our ferromagnetic ribbon. For a detailed exposition on the micromagnetic functional, we refer the reader to [5].

The micromagnetic energy functional comprises of the following components:

$$\mathcal{E}_{\text{magnetic}} = \underbrace{A\int_\Omega |\nabla \boldsymbol{m}(\boldsymbol{x})|^2 d\boldsymbol{x}}_{\mathcal{E}_{\text{ex}}} + \underbrace{K_a \int_\Omega \phi(\boldsymbol{m}) d\boldsymbol{x}}_{\mathcal{E}_{\text{anisotropy}}} + \underbrace{K_d \int_{\mathbb{R}^3} |\boldsymbol{h}_m|^2\, d\boldsymbol{x}}_{\mathcal{E}_{\text{demag.}}} - \underbrace{2K_d \int_\Omega \boldsymbol{h}_e \cdot \boldsymbol{m} d\boldsymbol{x}}_{\mathcal{E}_{\text{Zeeman}}}, \tag{6}$$

where $\mathcal{E}_{\text{ex}}$ denotes the exchange energy, $\mathcal{E}_{\text{anisotropy}}$ the magnetocrystalline anisotropy energy, $\mathcal{E}_{\text{demag.}}$ is the demag. energy, and $\mathcal{E}_{\text{Zeeman}}$ is the Zeeman energy. We now briefly discuss each energy component in the magnetic energy functional.

The Zeeman energy in minimised when magnetisation vector $\boldsymbol{m}$ is parallel and aligned along the external magnetic field $\boldsymbol{h}_e$, and is expressed as follows for the ribbon:

$$\mathcal{E}_{\text{Zeeman}} = -2K_d at \int_0^l \boldsymbol{h}_e \cdot \boldsymbol{m}(s) ds. \tag{7}$$

The magnetocrystalline anisotropy energy governs the favoured orientations for the magnetisation vector within the ferromagnetic sample, and assumes the following form:

$$\mathcal{E}_{\text{anisotropy}} = K_a \int_\Omega \left(1 - (\boldsymbol{m}(s) \cdot \boldsymbol{p}(s))^2\right) d\tilde{t} d\tilde{a} ds = K_a at \int_0^l \left(1 - (\boldsymbol{m}(s) \cdot \boldsymbol{p}(s))^2\right) ds, \tag{8}$$

where the material parameter K_a is known as the anisotropy constant, and $\boldsymbol{p}(s)$ is the easy axis. We have the following two scenarios:

- *Case 1. (soft ferromagnet)*: Here, $K_a \ll K_d$ indicates that the magnetocrystalline anisotropy energy is negligible. As a result, the magnetization has no preferred direction of orientation and aligns parallel to the external magnetic field $\boldsymbol{h}_e$ for a moderate external field. Since the external magnetic field $\boldsymbol{h}_e$ is applied along the $\boldsymbol{e}_2$ direction, we assume that $\boldsymbol{m}(\boldsymbol{x}) = \boldsymbol{m}(s) = \boldsymbol{e}_2$ for a soft ferromagnetic ribbon.
- *Case 2. (hard ferromagnet)*: Here, $K_a \gg K_d$ indicates that the magnetocrystalline anisotropy energy is very large. In this case, the magnetization vector makes a fixed angle with the tangent along the length of the ribbon. This can be expressed as $\boldsymbol{m}(\boldsymbol{x}) = \boldsymbol{m}(s) = \boldsymbol{p}(s) \in \{\boldsymbol{t}(s), \boldsymbol{n}(s)\}$.

The exchange energy penalises the gradient of the magnetisation and is expressed as follows:

$$\mathcal{E}_{ex} = A \int_{\Omega} |\nabla \boldsymbol{m}(\boldsymbol{x})|^2 d\tilde{t} d\tilde{a} ds = A \int_{s=0}^{l} \int_{\tilde{a}=-a/2}^{a/2} \int_{\tilde{t}=-t/2}^{t/2} |\nabla \boldsymbol{m}(\boldsymbol{x})|^2 d\tilde{t} d\tilde{a} ds, \tag{9}$$

where A is a material parameter known as the exchange constant.

We consider the representation of magnetisation distribution in material frame basis, that is, $\boldsymbol{m}(s)|_{\{\boldsymbol{d}_i\}} = \big(\boldsymbol{m}(s) \cdot \boldsymbol{d}_1(s), \boldsymbol{m}(s) \cdot \boldsymbol{d}_2(s), \boldsymbol{m}(s) \cdot \boldsymbol{d}_3(s)\big) = \big(m_{d_1}(s), m_{d_2}(s), m_{d_3}(s)\big)$. Incorporating this into Eqn. (9), the exchange energy expression reduces to

$$\begin{aligned}\mathcal{E}_{ex} =& Aa \int_{s=0}^{l} \int_{\tilde{t}=-t/2}^{t/2} \frac{1}{(1+\kappa\tilde{t})^2} \left[\left(\frac{\partial m_{d_1}}{\partial s} \right)^2 + \left(\frac{\partial m_{d_2}}{\partial s} - \kappa m_{d_3} \right)^2 \right. \\ & \left. + \left(\frac{\partial m_{d_3}}{\partial s} + \kappa m_{d_2} \right)^2 \right] d\tilde{t} ds, \qquad (10) \\ =& 4Aat \int_{s=0}^{l} \frac{1}{(4-\kappa^2 t^2)} \left[\left(\frac{\partial m_{d_1}}{\partial s} \right)^2 + \left(\frac{\partial m_{d_2}}{\partial s} - \kappa m_{d_3} \right)^2 + \left(\frac{\partial m_{d_3}}{\partial s} + \kappa m_{d_2} \right)^2 \right] ds. \qquad (11)\end{aligned}$$

Given the non-negativity of the exchange energy, the integrand of Eqn. (11) implies that $\kappa(s) < 2/t$. By retaining the leading-order terms in thickness (t), the exchange energy can be expressed as follows:

$$\begin{aligned}\mathcal{E}_{ex} &= Aat \int_0^l \left[\left(\frac{\partial m_{d_1}}{\partial s} \right)^2 + \left(\frac{\partial m_{d_2}}{\partial s} - \kappa m_{d_3} \right)^2 + \left(\frac{\partial m_{d_3}}{\partial s} + \kappa m_{d_2} \right)^2 \right] ds + \mathcal{O}(t^2) \\ &= Aat \int_0^l \Bigg[\underbrace{\left(\frac{\partial m_{d_1}}{\partial s} \right)^2 + \left(\frac{\partial m_{d_2}}{\partial s} \right)^2 + \left(\frac{\partial m_{d_3}}{\partial s} \right)^2}_{\text{isotropic}} \\ &\quad + \underbrace{2\kappa \left(m_{d_2} \frac{\partial m_{d_3}}{\partial s} - m_{d_3} \frac{\partial m_{d_2}}{\partial s} \right)}_{\text{chiral}} + \underbrace{\kappa^2 \left(m_{d_2}^2 + m_{d_3}^2 \right)}_{\text{anisotropic}} \Bigg] ds + \mathcal{O}(t^2). \qquad (12)\end{aligned}$$

We recover the isotropic, chiral and anisotropic components of the exchange energy, which are extensively documented in the literature on curvilinear micromagnetics [25, 29].

The detailed derivation of exchange energy is given in Appendix B. We now write down the demag. energy of the planar ferromagnetic ribbon. The demag. energy associated with planar ribbon is computed by solving Maxwell's equations of magnetostatics, namely,

$$\begin{aligned} \nabla \times \boldsymbol{h}_m(\boldsymbol{x}) &= \boldsymbol{0}, \\ \nabla \cdot (\boldsymbol{h}_m(\boldsymbol{x}) + \boldsymbol{m}(\boldsymbol{x})) &= 0. \end{aligned} \tag{13}$$

Here, $\boldsymbol{m}(\boldsymbol{x})$ is the magnetisation vector defined on the ferromagnetic body and is equal to zero outside the body. The field induced due to the magnetisation $\boldsymbol{m}(\boldsymbol{x})$ is denoted by $\boldsymbol{h}_m(\boldsymbol{x})$. The induced magnetic field $\boldsymbol{h}_m(\boldsymbol{x})$ can be found by solving Maxwell's equations of magnetostatics.

The demag. energy is evaluated by computing the square of the L^2-norm of $\boldsymbol{h}_m(\boldsymbol{x})$ on all of $\mathbb{R}^3$, it can be conveniently calculated in terms of Fourier transform of $\boldsymbol{m}(\boldsymbol{x})$, as follows:

$$\mathcal{E}_{\text{demag.}} = K_d \int_{\mathbb{R}^3} |\boldsymbol{h}_m|^2 \, d\boldsymbol{x} = K_d \int_{\mathbb{R}^3} \frac{\left|\widehat{\nabla \cdot \boldsymbol{m}}(\boldsymbol{\xi})\right|^2}{|\boldsymbol{\xi}|^2} d\boldsymbol{\xi}, \tag{14}$$

where $K_d = \frac{M_s^2}{2\mu_0}$ is the magnetostatic energy constant, M_s is the saturation magnetization of the material, and μ_0 is the permeability of the free space. We carry out the above integration in the material frame $(\boldsymbol{d}_1(s), \boldsymbol{d}_2(s), \boldsymbol{d}_3(s))$. In the material frame, $\boldsymbol{x} \mapsto \boldsymbol{r}(s) + \tilde{a}\boldsymbol{d}_1(s) + \tilde{t}\boldsymbol{d}_2(s)$, and $s \in [0, l]$, $\tilde{a} \in [-a/2, a/2]$, $\tilde{t} \in [-t/2, t/2]$, and $\boldsymbol{r}'(s) = \boldsymbol{d}_3(s)$. The Fourier transform of $\boldsymbol{m}$ in the material frame as follows:

$$\begin{aligned} \widehat{\nabla \cdot \boldsymbol{m}}(\boldsymbol{\xi}) &= \int_\Omega (\nabla \cdot \boldsymbol{m}) \exp(-i2\pi \boldsymbol{x} \cdot \boldsymbol{\xi}) d\boldsymbol{x} \\ &= \int_\Omega \frac{1}{J} \left(\partial_{\tilde{a}} m_{d_1} + \partial_{\tilde{t}} m_{d_2} + \partial_s m_{d_3} + \kappa[\tilde{t}\partial_{\tilde{a}} m_{d_1} + \tilde{t}\partial_{\tilde{t}} m_{d_2} + m_{d_2}] \right) \\ &\quad \times \exp\left(-i2\pi(s\xi_{d_3} + \tilde{a}\xi_{d_1} + \tilde{t}\xi_{d_2})\right) J \, ds d\tilde{a} d\tilde{t}. \end{aligned} \tag{15}$$

Here, J $(= 1 + \tilde{t}\kappa(s))$ is the Jacobian involved in computing the divergence of $\boldsymbol{m}$ and in the change of variables from (x_1, x_2, x_3) to $(s, \tilde{a}, \tilde{t})$. Furthermore, $m_{d_i} = \boldsymbol{m} \cdot \boldsymbol{d}_i(s)$, $\xi_{d_i} = \boldsymbol{\xi} \cdot \boldsymbol{d}_i(s)$. Since the ribbon under study is narrow, we shall assume $\boldsymbol{m}(\boldsymbol{x}) = \boldsymbol{m}(s)$ and in the above computation, the leading order term $(\mathcal{O}(t))$ of magnetostatic or demag. energy simplifies as follows:

$$\begin{aligned} \mathcal{E}_{\text{demag.}} &= K_d a t \int_{\mathbb{R}} \left|\widehat{m_{d_3}}(\xi_{d_2})\right|^2 d\xi_{d_3} = K_d a t \int_0^l (m_{d_2}(s))^2 ds \\ &= K_d a t \int_0^l (\boldsymbol{m}(s) \cdot \boldsymbol{d}_2(s))^2 ds. \end{aligned} \tag{16}$$

Details of the above calculation and other computations involved in deriving the leading order demag. energy can be found in Appendix A.

2.3 Total Energy of Ferromagnetic Elastic Ribbon

The total energy is the sum of $\mathcal{E}_{\text{elastica}}$ (Eqn. (4)) and $\mathcal{E}_{\text{magnetic}}$ (Eqns. (9), (8), (16), and (7)), and is given by the following expression:

$$\begin{aligned}\mathcal{E}(\theta, \boldsymbol{m}) = \frac{EI}{2}\int_0^l \left(\frac{\mathrm{d}\theta(s)}{\mathrm{d}s}\right)^2 ds + P\left(l - \int_0^l \cos\theta(s) ds\right) \\ + A\int_{s=0}^{l}\int_{\tilde{a}=-a/2}^{a/2}\int_{\tilde{t}=-t/2}^{t/2} |\nabla \boldsymbol{m}(s)|^2 d\tilde{t}d\tilde{a}ds \\ + K_a at\int_0^l \left(1 - (\boldsymbol{m}(s)\cdot\boldsymbol{p}(s))^2\right) ds + K_d at\int_0^l (\boldsymbol{m}(s)\cdot\boldsymbol{n}(s))^2 ds \\ - 2K_d at\int_0^l \boldsymbol{h}_e\cdot\boldsymbol{m}(s) ds. \end{aligned} \tag{17}$$

Incorporating the integral constraint (Eqn. (5)) with the help of a Lagrange multiplier R, the augmented energy functional for the elastic ferromagnetic ribbon is expressed as

$$\begin{aligned}\mathcal{E}(\theta, \boldsymbol{m}) = \frac{EI}{2}\int_0^l \left(\frac{\mathrm{d}\theta(s)}{\mathrm{d}s}\right)^2 ds + A\int_{s=0}^{l}\int_{\tilde{a}=-a/2}^{a/2}\int_{\tilde{t}=-t/2}^{t/2} |\nabla \boldsymbol{m}(s)|^2 d\tilde{t}d\tilde{a}ds \\ + K_a at\int_0^l \left(1 - (\boldsymbol{m}(s)\cdot\boldsymbol{p}(s))^2\right) ds + K_d at\int_0^l (\boldsymbol{m}(s)\cdot\boldsymbol{n}(s))^2 ds \\ - 2K_d at\int_0^l \boldsymbol{h}_e\cdot\boldsymbol{m}(s) ds + P\left(l - \int_0^l \cos\theta(s) ds\right) - R\int_0^l \sin\theta(s) ds. \end{aligned} \tag{18}$$

Non-dimensionalising the augmented energy functional gives:

$$\begin{aligned}\bar{\mathcal{E}}(\theta, \boldsymbol{m}) = \frac{\mathcal{E}(\theta, \boldsymbol{m})}{EI/l} \\ = \frac{1}{2}\int_0^1 \left(\theta'(\bar{s})\right)^2 d\bar{s} + \bar{A}\int_0^1\int_{\bar{a}=-1/2}^{1/2}\int_{\bar{t}=-1/2}^{1/2} |\nabla \boldsymbol{m}(\bar{s})|^2 d\bar{t}d\bar{a}d\bar{s} \\ + \bar{K}_a\int_0^1 \left(1 - (\boldsymbol{m}(\bar{s})\cdot\boldsymbol{p}(\bar{s}))^2\right) d\bar{s} + \bar{K}_d\int_0^1 (\boldsymbol{m}(\bar{s})\cdot\boldsymbol{n}(\bar{s}))^2 d\bar{s} \\ - 2\bar{K}_d\int_0^1 \boldsymbol{h}_e\cdot\boldsymbol{m}(\bar{s}) d\bar{s} + \bar{P}\left(1 - \int_0^1 \cos\theta(\bar{s}) d\bar{s}\right) - \bar{R}\int_0^1 \sin\theta(\bar{s}) d\bar{s}. \end{aligned} \tag{19}$$

where, $\bar{A}$, $\bar{K}_a$, $\bar{K}_d$, $\bar{P}$ and $\bar{R}$ are non-dimensional parameters defined as follows

$$\bar{A} = \frac{Aat/l}{EI/l} = \frac{12A}{Et^2}, \quad \bar{K}_a = \frac{K_a atl^2}{EI}, \quad \bar{K}_d = \frac{K_d atl^2}{EI} = \frac{12K_d}{E}\left(\frac{l}{t}\right)^2,$$

$$\bar{P} = \frac{Pl^2}{EI}, \text{ and } \quad \bar{R} = \frac{Rl^2}{EI},$$

while $\bar{a} = \frac{\tilde{a}}{a}$, and $\bar{t} = \frac{\tilde{t}}{t}$. Note that $\bar{K}_d$ and $\bar{K}_a$ are the two important non-dimensional numbers in our analysis; $\bar{K}_d$ represents the ratio of the demag. energy and the elastic energy, and

$\bar{K}_a$ denotes the ratio of the anisotropy energy and the elastic energy of the ferromagnetic ribbon. They depend on the material properties and the aspect ratio ($\frac{t}{l}$) of the ferromagnetic ribbon.

3 Equilibrium Equations

We will now derive the total energy functional and the corresponding Euler-Lagrange equations for two scenarios: 1. soft ferromagnetic ribbon and 2. hard ferromagnetic ribbon.

3.1 Soft Ferromagnetic Ribbon: $\left(K_a at \ll K_d at \sim \frac{EI}{l}\right)$ or ($\bar{K}_a \to 0$ and $\bar{K}_d \sim \mathcal{O}(1)$)

A soft ferromagnet is defined as a ferromagnet in which the anisotropy energy can be neglected [4]. The magnetisation vector does not have a preferred direction of alignment within the ferromagnetic solid. As a result, when the externally applied magnetic field is sufficiently large, the magnetization vector rotates to align with the field (Fig. 3). This alignment can be expressed as $\boldsymbol{m}(\bar{s}) \parallel \boldsymbol{h}_e$, leading to $\boldsymbol{m}(\bar{s}) = \boldsymbol{m}$, where $\boldsymbol{m}$ is a constant vector. For the case when external magnetic field is oriented along $\boldsymbol{e}_2$-axis, that is, $\boldsymbol{h}_e = h_e \boldsymbol{e}_2$, we have $\boldsymbol{m}(\bar{s}) = \boldsymbol{e}_2$. Here, h_e denotes the strength of the externally applied magnetic field.

Hence, the total energy of a soft ferromagnetic ribbon is given by

$$\begin{aligned}\bar{\mathcal{E}}(\theta) = \frac{1}{2}\int_0^1 \left(\theta'(\bar{s})\right)^2 d\bar{s} + \bar{A}\int_0^1 \int_{\bar{a}=-1/2}^{1/2}\int_{\bar{t}=-1/2}^{1/2} \underbrace{|\nabla \boldsymbol{m}|^2}_{=0} d\bar{t}\,d\bar{a}\,d\bar{s} \\ + \bar{K}_d \int_0^1 \cos^2\theta(\bar{s}) d\bar{s} + \bar{P}\int_0^1 \cos\theta(\bar{s}) d\bar{s} \\ - \bar{R}\int_0^1 \sin\theta(\bar{s}) d\bar{s} - \underbrace{(\bar{P} + 2\bar{K}_d h_e)}_{\text{constant}}.\end{aligned} \tag{20}$$

For a constant magnetisation $\boldsymbol{m}$, the exchange energy is zero, and the Zeeman energy remains constant. Consequently, the deformation in this case is driven by the interplay among demag. energy, bending energy, and loading device energy. By ignoring the constant terms, we obtain the total energy expression for the soft ferromagnetic ribbon as follows:

$$\bar{\mathcal{E}}(\theta) = \int_0^1 \left[\frac{1}{2}\left(\theta'(\bar{s})\right)^2 + \bar{K}_d \cos^2\theta(\bar{s}) + \bar{P}\cos\theta(\bar{s}) - \bar{R}\sin\theta(\bar{s})\right] d\bar{s}. \tag{21}$$

We now derive the corresponding Euler-Lagrange equations using tools from the calculus of variations. We assume that $\theta(\bar{s})$ is an extremizer of $\bar{\mathcal{E}}(\theta)$. We then introduce a small perturbation $\epsilon\eta(\bar{s})$ to the equilibrium solution $\theta(\bar{s})$, where ϵ is a positive scalar such that $\epsilon \ll 1$, and $\eta(\bar{s})$ is an admissible variation which satisfies the prescribed kinematic constraints. Next, we compute the first variation (or Gateaux derivative [6]) $\delta\bar{\mathcal{E}}(\theta;\eta)$ of $\mathcal{E}$ at θ along the direction η. This is computed as follows:

$$\begin{aligned}\delta\bar{\mathcal{E}}(\theta;\eta) &= \frac{\mathrm{d}}{\mathrm{d}\epsilon}\bar{\mathcal{E}}(\theta+\epsilon\eta)\Big|_{\epsilon=0} \\ &= \int_0^1 \left[\theta'(\bar{s})\eta'(\bar{s}) - \bar{K}_d \sin 2\theta(\bar{s})\eta(\bar{s} - \bar{P}\sin\theta(\bar{s})\eta(\bar{s}) - \bar{R}\cos\theta(\bar{s})\eta(\bar{s})\right] d\bar{s}.\end{aligned} \tag{22}$$

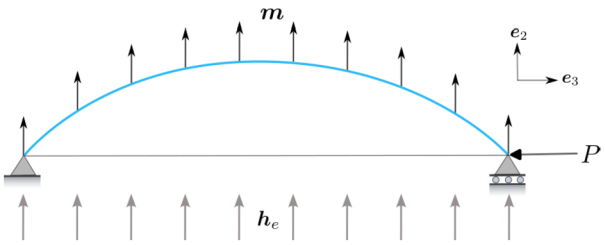


Fig. 3 Soft ferromagnetic ribbon under the influence of a transverse external magnetic field

By applying integration by parts and setting the Gateaux derivative, $\delta\mathcal{E}(\theta;\eta)$, to zero, we derive the following simplified expression:

$$\delta\bar{\mathcal{E}}(\theta;\eta) = \theta'(\bar{s})\eta'(\bar{s})\Big|_0^1 - \int_0^1 \left[\theta''(\bar{s}) + \bar{K}_d \sin 2\theta(\bar{s}) + \bar{P}\sin\theta(\bar{s}) + \bar{R}\cos\theta(\bar{s})\right]\eta(\bar{s})d\bar{s} = 0. \tag{23}$$

Finally, using the fundamental lemma of the calculus of variations, we derive the Euler-Lagrange equations, which represent the equilibrium conditions for a soft ferromagnetic ribbon. The corresponding equations, along with the generic boundary conditions, are expressed as follows:

$$\begin{aligned} \theta''(\bar{s}) + \bar{K}_d \sin 2\theta(\bar{s}) + \bar{P}\sin\theta(\bar{s}) + \bar{R}\cos\theta(\bar{s}) &= 0, \\ \theta'(\bar{s})\eta(\bar{s})|_{\bar{s}=0} &= 0, \\ \theta'(\bar{s})\eta(\bar{s})|_{\bar{s}=1} &= 0, \end{aligned} \tag{24}$$

subject to the constraint:

$$\bar{y}(1) = \int_0^1 \sin\theta(\bar{s})\, d\bar{s} = 0. \tag{25}$$

When $\bar{K}_d = 0$, we obtain the equilibrium equation for the classical Euler's elastica as follows:

$$\theta''(\bar{s}) + \bar{P}\sin\theta(\bar{s}) + \bar{R}_e\cos\theta(\bar{s}) = 0, \tag{26}$$

where $\bar{R}_e$ denotes $\bar{R}$-value for the Euler's elastica.

We consider three canonical boundary conditions for our analysis, namely

- fixed-free: $\theta(\bar{s}=0) = 0$, $\theta'(\bar{s}=1) = 0$,
- fixed-fixed: $\theta(\bar{s}=0) = 0$, $\theta(\bar{s}=1) = 0$,
- pinned-pinned: $\theta'(\bar{s}=0) = 0$, $\theta'(\bar{s}=1) = 0$.

Note that the constraint (Eqn. (25)) does not apply for fixed-free condition.

3.2 Hard Ferromagnetic Ribbon: $\left(K_d at \ll K_a at \sim \frac{EI}{l} \sim K_d at h_e\right)$ or $(\bar{K}_d \to 0,$ $\bar{K}_d h_e \sim \mathcal{O}(1)$ and $\bar{K}_a \sim \mathcal{O}(1))$

A hard ferromagnet is a ferromagnet with very large magnetic anisotropy energy ($K_a \gg 1$). The magnetic anisotropy energy is minimised when the magnetization vector aligns along

a preferred direction within the ferromagnetic solid. Thus, in a hard ferromagnetic ribbon, magnetization vector $\boldsymbol{m}(\bar{s})$ makes a constant angle with the tangent ($\boldsymbol{d}_3(\bar{s})$) along the entire length of the ribbon. As the ribbon deforms, $\boldsymbol{m}(\bar{s})$ varies spatially to maintain this constant angle with the tangent of the ribbon centerline. In this case, the direction of magnetization reorients in response to the induced deformation caused by the presence of the external magnetic field $\boldsymbol{h}_e$.

As the magnetisation maintains a constant angle with respect to the tangent to the centerline, the components of $\boldsymbol{m}(\bar{s})$ in material frame basis remain constant, that is, $\frac{\partial m_{d_i}}{\partial \bar{s}} = 0$, $i = 1, 2, 3$. Incorporating these in Eqn. (12), we obtain the form of exchange energy as:

$$\mathcal{E}_{ex} = Aat \int_0^l \kappa^2 \left[\left(m_{d_2}\right)^2 + \left(m_{d_3}\right)^2 \right] ds. \tag{27}$$

We will consider that $\boldsymbol{m}(\bar{s})$ is either aligned along the normal ($\boldsymbol{m}(\bar{s}) \perp \boldsymbol{d}_2(\bar{s})$) or that it is aligned along the tangent ($\boldsymbol{m}(\bar{s}) \parallel \boldsymbol{d}_3(\bar{s})$) of the centerline curve $\boldsymbol{r}(\bar{s})$, see Figs. 4a and 4b. Accordingly, the components of $\boldsymbol{m}(\bar{s})$ are $(m_{d_1}, m_{d_2}, m d_3) = (0, 1, 0)$ or $(0, 0, 1)$, for normal or tangential magnetisation distributions respectively. For either case, exchange energy expression reduces to

$$\mathcal{E}_{ex} = Aat \int_0^l \kappa^2 ds. \tag{28}$$

Non-dimensionalising it with respect to EI/l, in the same manner as Eqn. (19), results in

$$\bar{\mathcal{E}}_{ex}(\theta) = \frac{\mathcal{E}_{ex}(\theta)}{EI/l} = \bar{A} \int_0^1 \left(\theta'(\bar{s})\right)^2 d\bar{s}. \tag{29}$$

Also, the magnetisation is aligned along the easy axis, such that $\boldsymbol{m}(s) = \boldsymbol{p}(s) \in \{\boldsymbol{t}(s), \boldsymbol{n}(s)\}$. Due to the unity nature of $\boldsymbol{m}(\bar{s})$, that is, $|\boldsymbol{m}(s)| = 1$, we adopt the following general expression for $\boldsymbol{m}(\bar{s})$ in the Cartesian representation:

$$\boldsymbol{m}(\bar{s}) = (0, \sin\phi(\bar{s}), \cos\phi(\bar{s})), \tag{30}$$

where $\phi(\bar{s})$ is the angle between $\boldsymbol{m}(\bar{s})$ and $\boldsymbol{e}_3$ at $\bar{s}$. The transverse external magnetic field can be represented as $\boldsymbol{h}_e = h_e \boldsymbol{e}_2$ or $\boldsymbol{h}_e = -h_e \boldsymbol{e}_2$ depending on whether the field is applied along positive or negative $\boldsymbol{e}_2$-direction. Upon substituting the expressions of $\boldsymbol{m}(\bar{s})$ (Eqn. (30)) and the exchange energy (Eqn. (29)) in Eqn. (19), we obtain

$$\begin{aligned}
\bar{\mathcal{E}}(\theta, \psi) = &\left(\frac{1}{2} + \bar{A}\right) \int_0^l \left(\theta'(\bar{s})\right)^2 d\bar{s} + \bar{K}_a \int_0^1 \underbrace{\left(1 - (\boldsymbol{m}(\bar{s}) \cdot \boldsymbol{p}(\bar{s}))^2\right)}_{=0} d\bar{s} \\
&+ \bar{K}_d \int_0^1 \underbrace{(\boldsymbol{m}(\bar{s}) \cdot \boldsymbol{n}(\bar{s}))^2}_{\text{constant}} d\bar{s} + \bar{P} \int_0^1 \cos\theta(\bar{s}) d\bar{s} \\
&\mp 2\bar{K}_d h_e \int_0^1 \sin\phi(\bar{s}) d\bar{s} - \bar{Q} \int_0^1 \sin\theta(\bar{s}) d\bar{s} - \underbrace{\bar{P}}_{\text{constant}}.
\end{aligned} \tag{31}$$

where $\bar{Q}$ is a Lagrange multiplier introduced to distinguish from $\bar{R}$ or $\bar{R}_e$. Recall $\bar{R}_e$ is the vertical reaction for the Euler's elastica (see Eqn. (26)).

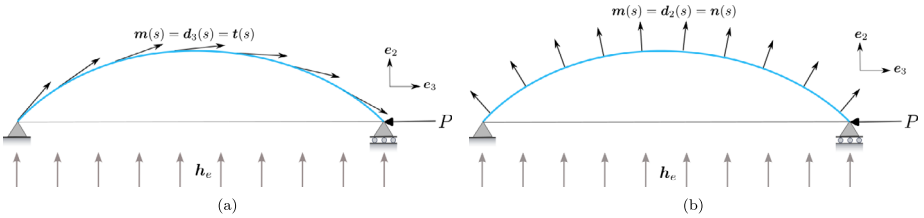


Fig. 4 Hard ferromagnetic ribbon under the influence of an external magnetic field: (a) Magnetization along the tangential direction, (b) Magnetization along the normal direction

Note that, in this case $(\boldsymbol{m}(\bar{s}) \cdot \boldsymbol{n}(\bar{s}))^2$ is constant and hence the demag. energy does not participate in energy minimization. The large value of K_a ensures that $\boldsymbol{m}(\bar{s})$ is parallel and aligned along $\boldsymbol{p}(\bar{s})$. The contribution of exchange energy is negligible since $\bar{A} \ll 1$. Therefore, the deformation in this case is driven by the interplay among bending energy, loading device energy, and Zeeman energy. By omitting the constant terms, we get the total energy expression for the hard ferromagnetic ribbon as

$$\bar{\mathcal{E}}(\theta) = \int_0^1 \left[\frac{1}{2} \left(\theta'(\bar{s})\right)^2 + \bar{P} \cos\theta(\bar{s}) \mp 2\bar{K}_d h_e \sin\phi(\bar{s}) - \bar{Q} \sin\theta(\bar{s}) \right] d\bar{s}. \tag{32}$$

Following similar steps as in the soft magnetization scenario, we arrive at the Euler-Lagrange equations for the hard magnetization case, expressed as follows:

$$\begin{aligned} \theta''(\bar{s}) + \bar{P} \sin\theta(\bar{s}) \pm 2\bar{K}_d h_e \cos\phi(\bar{s}) + \bar{Q} \cos\theta(\bar{s}) = 0, \\ \theta'(\bar{s})\eta(\bar{s})|_{\bar{s}=0} = 0, \\ \theta'(\bar{s})\eta(\bar{s})|_{\bar{s}=1} = 0. \end{aligned} \tag{33}$$

We consider two types of uniform magnetization distributions: tangential and normal. For tangential magnetization, we have $\phi(\bar{s}) = \theta(\bar{s})$, while for normal magnetization, $\phi(\bar{s}) = \theta(\bar{s}) + \frac{\pi}{2}$ (see Fig. 4). Also, we expose the hard ferromagnetic ribbon to a transverse external magnetic field, represented by $\boldsymbol{h}_e = h_e \boldsymbol{e}_2$ and $\boldsymbol{h}_e = -h_e \boldsymbol{e}_2$. The corresponding equilibrium equations are listed below:

$$\begin{aligned} \boldsymbol{h}_e = \pm h_e \boldsymbol{e}_2 : \boldsymbol{m}(\bar{s}) = \boldsymbol{t}(\bar{s}) : \quad \theta''(\bar{s}) + \bar{P} \sin\theta(\bar{s}) + (\bar{Q} \pm 2\bar{K}_d h_e) \cos\theta(\bar{s}) = 0, \\ \boldsymbol{m}(\bar{s}) = \boldsymbol{n}(\bar{s}) : \quad \theta''(\bar{s}) + (\bar{P} \mp 2\bar{K}_d h_e) \sin\theta(\bar{s}) + \bar{Q} \cos\theta(\bar{s}) = 0. \end{aligned} \tag{34}$$

3.3 Comparison of Our Model Against Moon et al. [19]

The work conducted by Moon et al. [19] involved a cantilevered Euler beam with hard magnetization (see Fig. 5). We consider the equilibrium equation for a hard ferromagnetic ribbon with tangential magnetization (Eqn. $(34)_1$) subjected to pure magnetic loading under fixed-free boundary conditions, with the parameters set to $\bar{Q} = \bar{P} = 0$, as follows:

$$\theta''(\bar{s}) + 2\bar{K}_d h_e \sin\theta(\bar{s}) = 0 \tag{35}$$

The above equation matches with the hard cantilevered Euler beam considered in Wang et al. [30]. We linearise Eqn. (35) about the undeformed configuration $\theta(\bar{s}) = 0$. From the

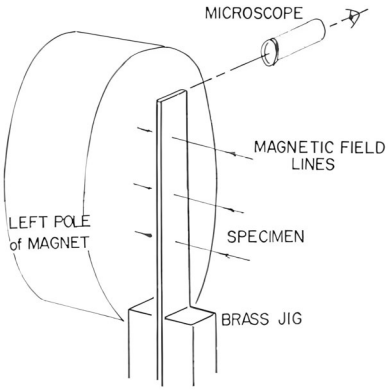


Fig. 5 Cantilevered beam immersed in magnetic field; adapted from [19]

non-dimensionalised arclength parametrisation (Eqn. (3)), we have

$$\frac{\mathrm{d}\bar{y}}{\mathrm{d}\bar{s}} = \sin\theta(\bar{s}), \qquad \frac{\mathrm{d}\bar{z}}{\mathrm{d}\bar{s}} = \cos\theta(\bar{s}). \tag{36}$$

The small angle approximation, where $\theta(\bar{s}) \ll 1$, leads to the following results:

$$\cos\theta(\bar{z}) \approx 1, \ \bar{z} \approx \bar{s}, \ \sin\theta(\bar{z}) \approx \theta(\bar{z}). \tag{37}$$

Upon substituting Eqns. (37) in Eqn. (35), and differentiating it with respect to $\bar{z}$, we have

$$\frac{\mathrm{d}^3\theta}{\mathrm{d}\bar{z}^3} + 2\bar{K}_d h_e \frac{\mathrm{d}\theta}{\mathrm{d}\bar{z}} = 0. \tag{38}$$

From Eqns. (36), (37) and (38), we obtain the linearisation of Eqn. (35) as

$$\frac{\mathrm{d}^4\bar{y}}{\mathrm{d}\bar{z}^4} + 2\bar{K}_d h_e \frac{\mathrm{d}^2\bar{y}}{\mathrm{d}\bar{z}^2} = 0, \tag{39}$$

which is identical to the equation presented in Moon et al. [19]. Furthermore, the critical magnetic load varies as

$$(K_d h_e)_c \sim \left(\frac{t}{l}\right)^2. \tag{40}$$

We can also recover all the critical loads as well as the deformation modeshapes presented in Table 1 of Moon et al. [19].

4 Path Continuation Methodology

We outline the numerical methodology used to obtain solutions to the equilibrium equations as the loading parameter $\bar{P}$ is quasi-statically varied for various loading scenarios. We use a numerical continuation method called pseudo arc length-based technique, as discussed in [20] to determine the deformed configurations. This technique constrains the incremental deformation measures and the increments in load parameters ($\bar{P}$, $\bar{R}$) using a hyperspheric constraint.

4.1 Discretization of Equilibrium Equations

Before initiating the numerical continuation procedure, we first discretize the equilibrium equation of the ferromagnetic ribbon for a specific loading scenario using finite difference method. Here, we consider a soft ferromagnetic ribbon with fixed-fixed boundary conditions. We discretize the equilibrium equation, as given in Eqn. (24). The domain is divided into $(N+2)$ nodal points, defined as $\bar{s}_i = ih$ for $i = 0, 1, \ldots, N+1$, where the uniform spacing is given by $h = \frac{1}{N+1}$. To approximate the second-order derivative in Eqn. (24), we employ second-order accurate central difference scheme. The resulting discrete system of equations, along with the boundary conditions, is given by:

$$\begin{gathered}\frac{\theta_{i-1} - 2\theta_i + \theta_{i+1}}{h^2} + \bar{P}\sin\theta_i + \bar{K}_d \sin 2\theta_i + \bar{R}\cos\theta_i = 0; \qquad i = 1, 2, \ldots, N, \\ \theta_0 = 0, \theta_{N+1} = 0,\end{gathered} \tag{41}$$

where θ_i denotes the numerical counterpart of $\theta(\bar{s} = \bar{s}_i)$. In matrix-vector form, the discretized system can be written for all three boundary conditions (for the fixed-free case, $\bar{R} = 0$) as

$$\boldsymbol{K\theta} + \bar{P}\sin\boldsymbol{\theta} + \bar{K}_d \sin 2\boldsymbol{\theta} + \bar{R}\cos\boldsymbol{\theta} = \mathbf{0} \text{ (see Appendix C for } \boldsymbol{K} \text{ and } \boldsymbol{\theta}). \tag{42}$$

Incorporating the discretized form of the integral constraint (Eqn. (25)) results in a combined nonlinear system of equations for both fixed-fixed and pinned-pinned conditions, expressed as follows:

$$\begin{gathered}\begin{pmatrix} \boldsymbol{K\theta} + \bar{P}\sin\boldsymbol{\theta} + \bar{K}_d \sin 2\boldsymbol{\theta} + \bar{R}\cos\boldsymbol{\theta} \\ \sin\theta_1 + \cdots + \sin\theta_N \end{pmatrix} = \begin{pmatrix} \mathbf{0} \\ 0 \end{pmatrix}, \\ \text{or,} \qquad \boldsymbol{f}(\boldsymbol{\theta}, \bar{R}, \bar{P}) = \mathbf{0}.\end{gathered} \tag{43}$$

4.2 Pseudo Arc Length-Based Continuation Method

We devise a strategy to solve the nonlinear system of equations (Eqn. (43)) using the pseudo arc length-based continuation method. We describe the k-th configuration of the planar-deforming ferromagnetic ribbon as $(\boldsymbol{\theta}_k, \bar{R}_k, \bar{P}_k)$ where k denotes the configuration index. The algorithm works in two steps: prediction step and correction step.

Prediction Step : We expand the equilibrium equation (Eqn. (43)) at the $(k+1)$-th index using Taylor series expansion about the k-th index, resulting in:

$$\begin{aligned}\underbrace{\boldsymbol{f}(\boldsymbol{\theta}_{k+1}, \bar{R}_{k+1}, \bar{P}_{k+1})}_{=\mathbf{0}} &= \underbrace{\boldsymbol{f}(\boldsymbol{\theta}_k, \bar{R}_k, \bar{P}_k)}_{=\mathbf{0}} + \left.\frac{\partial \boldsymbol{f}}{\partial \boldsymbol{\theta}}\right|_k \Delta\boldsymbol{\theta}_k + \left.\frac{\partial \boldsymbol{f}}{\partial \bar{R}}\right|_k \Delta\bar{R}_k + \left.\frac{\partial \boldsymbol{f}}{\partial \bar{P}}\right|_k \Delta\bar{P}_k \\ &\quad + \underbrace{\mathcal{O}(\Delta\boldsymbol{\theta}_k^2, \Delta\bar{R}_k^2, \Delta\bar{P}_k^2)}_{\text{ignore}},\end{aligned} \tag{44}$$

$$\implies \left.\frac{\partial \boldsymbol{f}}{\partial \boldsymbol{\theta}}\right|_k \Delta\boldsymbol{\theta}_k + \left.\frac{\partial \boldsymbol{f}}{\partial \bar{R}}\right|_k \Delta\bar{R}_k + \left.\frac{\partial \boldsymbol{f}}{\partial \bar{P}}\right|_k \Delta\bar{P}_k = \mathbf{0}. \tag{45}$$

We define a tangent vector as

$$\boldsymbol{e}_k = \begin{pmatrix} \Delta\boldsymbol{\theta}_k \\ \Delta\bar{R}_k \\ \Delta\bar{P}_k \end{pmatrix}, \tag{46}$$

whose norm squared is

$$\|\boldsymbol{e}_k\|^2 = (\Delta\boldsymbol{\theta}_k)^T(\Delta\boldsymbol{\theta}_k) + (\Delta\bar{R}_k)^2 + (\Delta\bar{P}_k)^2. \tag{47}$$

We make the following substitution

$$\Delta\bar{P}_k = a_k,\ \Delta\bar{R}_k = a_k\Delta r_k,\ \Delta\boldsymbol{\theta}_k = a_k\Delta\boldsymbol{\phi}_k. \tag{48}$$

Setting the norm of $\boldsymbol{e}_k$ to unity, we obtain the hyperspheric constraint which yields an expression for a_k

$$a_k^2(\Delta\boldsymbol{\phi}_k)^T(\Delta\boldsymbol{\phi}_k) + a_k^2(\Delta r_k)^2 + a_k^2 = 1, \tag{49}$$

$$\implies a_k = \pm\frac{1}{\sqrt{(\Delta\boldsymbol{\phi}_k)^T(\Delta\boldsymbol{\phi}_k) + (\Delta r_k)^2 + 1}}. \tag{50}$$

The sign of a_k is chosen positive if $\boldsymbol{e}_{k-1}^T\boldsymbol{e}_k > 0$ or else a_k is taken to be negative. Substituting the expressions for $\Delta\boldsymbol{\theta}_k$, $\Delta\bar{R}_k$ and $\Delta\bar{P}_k$ in Eqn. (45), we have

$$\left.\frac{\partial\boldsymbol{f}}{\partial\boldsymbol{\theta}}\right|_k a_k\Delta\boldsymbol{\phi}_k + \left.\frac{\partial\boldsymbol{f}}{\partial\bar{R}}\right|_k a_k\Delta r_k + \left.\frac{\partial\boldsymbol{f}}{\partial\bar{P}}\right|_k a_k = \boldsymbol{0}, \tag{51}$$

$$\implies \begin{bmatrix} \left.\frac{\partial\boldsymbol{f}}{\partial\boldsymbol{\theta}}\right|_k & \left.\frac{\partial\boldsymbol{f}}{\partial\bar{R}}\right|_k \end{bmatrix} \begin{pmatrix} \Delta\boldsymbol{\phi}_k \\ \Delta r_k \end{pmatrix} = -\left.\frac{\partial\boldsymbol{f}}{\partial\bar{P}}\right|_k. \tag{52}$$

We use Eqn. (52) to solve for $\Delta\boldsymbol{\phi}_k$, Δr_k and then compute a_k (Eqn. (50)) and $\boldsymbol{e}_k$ (Eqn. (46)). We now construct the initial guess for $(k+1)$-configuration as

$$\begin{pmatrix} \boldsymbol{\theta}_{k+1}^{(0)} \\ \bar{R}_{k+1}^{(0)} \\ \bar{P}_{k+1}^{(0)} \end{pmatrix} = \begin{pmatrix} \boldsymbol{\theta}_k \\ \bar{R}_k \\ \bar{P}_k \end{pmatrix} + \Delta s \cdot \boldsymbol{e}_k, \tag{53}$$

where Δs is the radius of the hypersphere and the arc length step size. It is chosen to be sufficiently small to accurately capture the bifurcation along the equilibrium path.

Correction Step : We subject the predicted initial guess for the $(k+1)$-configuration (Eqn. (53))to a sequence of corrective iterations using the widely used Newton-Raphson technique. Denoting the $(k+1)$-configuration by $(\boldsymbol{\theta}_{k+1}, \bar{R}_{k+1}, \bar{P}_{k+1})$, we derive the following Taylor series expansion about the l-iteration level:

$$\underbrace{\boldsymbol{f}(\boldsymbol{\theta}_{k+1}, \bar{R}_{k+1}, \bar{P}_{k+1})}_{=\boldsymbol{0}} \approx \boldsymbol{f}(\boldsymbol{\theta}_{k+1}^{(l)}, \bar{R}_{k+1}^{(l)}, \bar{P}_{k+1}^{(l)}) + \left.\frac{\partial\boldsymbol{f}}{\partial\boldsymbol{\theta}}\right|_{k+1}^{(l)} \Delta\boldsymbol{\theta}_{k+1}^{(l+1)} + \left.\frac{\partial\boldsymbol{f}}{\partial\bar{R}}\right|_{k+1}^{(l)} \Delta\bar{R}_{k+1}^{(l+1)} + \left.\frac{\partial\boldsymbol{f}}{\partial\bar{P}}\right|_{k+1}^{(l)} \Delta\bar{P}_{k+1}^{(l+1)}, \tag{54}$$

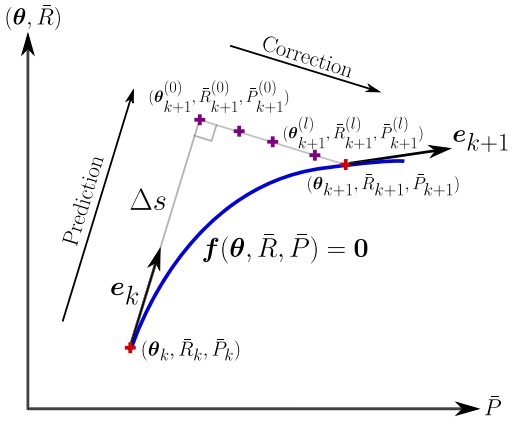


Fig. 6 Schematic of the pseudo arc length-based continuation procedure, illustrating a blue curve where each point represents an equilibrium configuration

$$\implies \left.\frac{\partial \boldsymbol{f}}{\partial \boldsymbol{\theta}}\right|^{(l)}_{k+1} \Delta\boldsymbol{\theta}^{(l+1)}_{k+1} + \left.\frac{\partial \boldsymbol{f}}{\partial \bar{R}}\right|^{(l)}_{k+1} \Delta\bar{R}^{(l+1)}_{k+1} + \left.\frac{\partial \boldsymbol{f}}{\partial \bar{P}}\right|^{(l)}_{k+1} \Delta\bar{P}^{(l+1)}_{k+1} = -\boldsymbol{f}(\boldsymbol{\theta}^{(l)}_{k+1}, \bar{R}^{(l)}_{k+1}, \bar{P}^{(l)}_{k+1}). \tag{55}$$

We impose the orthogonality constraint on the tangent vector at each iteration level l, which is expressed as:

$$\boldsymbol{e}^T_k \boldsymbol{e}^{(l+1)}_{k+1} = 0, \tag{56}$$

$$\implies (\Delta\boldsymbol{\theta}_k)^T(\Delta\boldsymbol{\theta}^{(l+1)}_{k+1}) + (\Delta\bar{R}_k)(\Delta\bar{R}^{(l+1)}_{k+1}) + (\Delta\bar{P}_k)(\Delta\bar{P}^{(l+1)}_{k+1}) = 0. \tag{57}$$

Combining Eqns. (55) and (57) to construct the following iterative scheme

$$\begin{bmatrix} \left.\frac{\partial \boldsymbol{f}}{\partial \boldsymbol{\theta}}\right|^{(l)}_{k+1} & \left.\frac{\partial \boldsymbol{f}}{\partial \bar{R}}\right|^{(l)}_{k+1} & \left.\frac{\partial \boldsymbol{f}}{\partial \bar{P}}\right|^{(l)}_{k+1} \\ (\Delta\boldsymbol{\theta}_k)^T & \Delta\bar{R}_k & \Delta\bar{P}_k \end{bmatrix} \begin{pmatrix} \Delta\boldsymbol{\theta}^{(l+1)}_{k+1} \\ \Delta\bar{R}^{(l+1)}_{k+1} \\ \Delta\bar{P}^{(l+1)}_{k+1} \end{pmatrix} = \begin{pmatrix} -\boldsymbol{f}(\boldsymbol{\theta}^{(l)}_{k+1}, \bar{R}^{(l)}_{k+1}, \bar{P}^{(l)}_{k+1}) \\ 0 \end{pmatrix}. \tag{58}$$

We solve the matrix equation (Eqn. (58)) and subsequently perform the update procedure:

$$\begin{pmatrix} \boldsymbol{\theta}^{(l+1)}_{k+1} \\ \bar{R}^{(l+1)}_{k+1} \\ \bar{P}^{(l+1)}_{k+1} \end{pmatrix} = \begin{pmatrix} \boldsymbol{\theta}^{(l)}_{k+1} \\ \bar{R}^{(l)}_{k+1} \\ \bar{P}^{(l)}_{k+1} \end{pmatrix} + \begin{pmatrix} \Delta\boldsymbol{\theta}^{(l+1)}_{k+1} \\ \Delta\bar{R}^{(l+1)}_{k+1} \\ \Delta\bar{P}^{(l+1)}_{k+1} \end{pmatrix}. \tag{59}$$

The correction steps ($l = 1, 2, \dots$) are carried out until the increments meet a prescribed tolerance. We then increment the configuration index ($k \leftarrow k+1$) and repeat the prediction and correction steps until $\bar{P}_{\max}$ is reached. The continuation procedure we adopted is depicted in Fig. 6.

5 Bifurcation Analysis of Equilibrium Configuration

We now evaluate the stability of a given deformed equilibrium configuration with respect to infinitesimal perturbations. We expect that stable perturbations will be physically realizable. To determine stability, we need to calculate the second variation of the energy functional at

the critical points. These critical points correspond to the solutions of the Euler-Lagrange equations.

We proceed to determine the second variation of the functional $\delta^2\bar{\mathcal{E}}(\theta)$ for a specific case of a soft ferromagnetic ribbon with fixed-fixed boundary conditions exposed to $\boldsymbol{h}_e$ applied along the $\boldsymbol{e}_2$-axis. We introduce a first-order perturbation in the assumed extremum θ, expressed as $\hat{\theta}(\bar{s}) = \theta(\bar{s}) + \epsilon\eta(\bar{s})$, where $\eta(\bar{s})$ is a kinematically admissible planar variation and ϵ is a small parameter, as discussed in Sect. 3.1. This perturbed quantity $\hat{\theta}(\bar{s})$ is then substituted into Eqn. (21):

$$\bar{\mathcal{E}}(\theta+\epsilon\eta) = \int_0^1 \Big[\frac{1}{2}\left(\theta'(\bar{s})+\epsilon\eta'(\bar{s})\right)^2 + \bar{K}_d\cos^2(\theta(\bar{s})+\epsilon\eta(\bar{s})) + \bar{P}\cos(\theta(\bar{s})+\epsilon\eta(\bar{s})) - \bar{R}\sin(\theta(\bar{s})+\epsilon\eta(\bar{s}))\Big]d\bar{s}. \tag{60}$$

By simplifying the above expansion and considering the boundary conditions, $\theta(0) = \theta(1) = \eta(0) = \eta(1) = 0$, we obtain:

$$\begin{aligned}\delta^2\bar{\mathcal{E}}(\theta) &= \frac{\mathrm{d}^2}{\mathrm{d}\epsilon^2}\bar{\mathcal{E}}(\theta+\epsilon\eta)\Big|_{\epsilon=0} \\ &= -\int_0^1 \left[\eta''(\bar{s}) + 2\bar{K}_d\cos 2\theta(\bar{s})\eta(\bar{s}) + \bar{P}\cos\theta(\bar{s})\eta(\bar{s}) - \bar{R}\sin\theta(\bar{s})\eta(\bar{s})\right]\eta(\bar{s})d\bar{s},\end{aligned} \tag{61}$$

for all kinematically admissible functions $\eta(\bar{s})$. The stability criterion states that

$$\delta^2\bar{\mathcal{E}}(\theta)\begin{cases} > 0 & \text{stable,} \\ < 0 & \text{unstable.}\end{cases} \tag{62}$$

Further, we also introduce the first variation of the integral constraint $\int_0^1 \sin\theta(\bar{s})d\bar{s} = 0$ given as:

$$\int_0^1 \cos\theta(\bar{s})\eta(\bar{s})d\bar{s} = 0. \tag{63}$$

5.1 Construction of Sturm-Liouville Problem

Following the work of [2, 15], we construct an equivalent Sturm-Liouville problem for the second variation $\delta^2\bar{\mathcal{E}}(\theta)$ (Eqn. (61)) as follows:

$$\phi_n''(\bar{s}) + \lambda_n L(\bar{s})\phi_n(\bar{s}) = C_{R_n}\cos\theta(\bar{s}), \tag{64}$$

where λ_n represents the eigenvalues, and ϕ_n denotes the corresponding eigenmodes of Eqn. (64). The term $L(\bar{s}) = (2\bar{K}_d\cos 2\theta(\bar{s}) + \bar{P}\cos\theta(\bar{s}) - \bar{R}\sin\theta(\bar{s}))$ serves as the weight function. Also, C_{R_n} is a Lagrange parameter introduced to enforce the isoperimetric constraint (Eqn. (63)). The conditions on $\phi_n(\bar{s})$ are

- fixed-fixed case: $\phi_n(0) = \phi_n(1) = 0$ and $\int_0^1 \cos\theta(\bar{s})\phi_n(\bar{s})d\bar{s} = 0$,
- pinned-pinned case: $\phi_n'(0) = \phi_n'(1) = 0$ and $\int_0^1 \cos\theta(\bar{s})\phi_n(\bar{s})d\bar{s} = 0$,
- fixed-free case: $\phi_n(0) = \phi_n'(1) = 0$.

We derive the following conditions for two arbitrary eigenmodes $\phi_m(\bar{s})$ and $\phi_n(\bar{s})$ of the Sturm-Liouville problem (Eqn. (64)):

$$\lambda_n \int_0^1 L(\bar{s})\phi_n^2(\bar{s})d\bar{s} = \int_0^1 \phi_n'^2 d\bar{s}, \tag{65}$$

and the orthogonality condition

$$\int_0^1 L(\bar{s})\phi_n(\bar{s})\phi_m(\bar{s})d\bar{s} = 0. \tag{66}$$

The details of the above calculation can be found in Appendix D.

Spectral Decomposition : We will use $\phi_n(\bar{s})$ along with the weight function $L(\bar{s})$ to construct a Fourier series representation (converging in the mean) of the square-integrable function $\eta(\bar{s})$,

$$\eta(\bar{s}) = \sum_{n=1}^{\infty} c_n \phi_n(\bar{s}), \qquad c_n \text{ are Fourier coefficients.} \tag{67}$$

By substituting the above representation into Eqn. (61) and applying the conditions from Eqns. (65) and (66), we obtain the stability criterion:

$$\delta^2\bar{\mathcal{E}}(\theta) = \sum_{n=1}^{\infty} c_n^2 \left(1 - \frac{1}{\lambda_n}\right) \int_0^1 (\phi_n'(\bar{s}))^2 d\bar{s} \quad \begin{cases} > 0 \text{ if } \lambda_n \notin [0,1] & \text{stable,} \\ < 0 \text{ if } \lambda_n \in [0,1] & \text{unstable.} \end{cases} \tag{68}$$

The detailed bifurcation analysis technique is presented in Appendix D.

5.1.1 Numerical Bifurcation Analysis

We describe the numerical procedure for the fixed-fixed case, which can be readily adapted for the pinned-pinned and fixed-free cases. Given Eqn. (64) as

$$\phi_m''(\bar{s}) + \lambda_m L_m(\bar{s})\phi_m(\bar{s}) = C_{R_m} N(\bar{s}), \tag{69}$$

where, the coefficient functions are

$$L_m(\bar{s}) = 2\bar{K}_d \cos 2\theta(\bar{s}) + \bar{P}\cos\theta(\bar{s}) - \bar{R}\sin\theta(\bar{s}), \qquad N(\bar{s}) = \cos\theta(\bar{s}). \tag{70}$$

Eqn. (69) is also subjected to the boundary conditions $\phi_m(0) = 0$, $\phi_m(1) = 0$ and the additional constraint

$$\int_0^1 \phi_m(\bar{s})N(\bar{s})d\bar{s} = 0. \tag{71}$$

Numerical Procedure to Compute Eigenvalues λ_m : Partition the interval $\bar{s} \in [0,1]$ into segments of equal length $h = \frac{1}{n+1}$, where the starting points of the segments are denoted by $\bar{s}_{i-1} = (i-1)h$ for $i = 1, 2, \ldots, n+1$. For the i-th segment, the functions $L(\bar{s})$ and $N(\bar{s})$ are approximated by averaging their corresponding values at the nodal indices i and $i+1$,

resulting in the quantities L_i and N_i, respectively. Substituting these averaged values, Eqn. (69) becomes

$$\phi_m''(\bar{s}) + \lambda_m L_i \phi_m(\bar{s}) = C_{R_m} N_i, \tag{72}$$

which is an ordinary differential equation (ODE) with constant coefficients. The solution to this ODE is given by

$$\phi_m(\bar{s}) = A_{1i} F_{1i}(\bar{s} - \bar{s}_{i-1}) + A_{2i} F_{2i}(\bar{s} - \bar{s}_{i-1}) + C_{R_m} \frac{N_i}{\lambda_m L_i}, \tag{73}$$

where A_{1i} and A_{2i} are constants, and the functions F_{1i} and F_{2i} are defined as follows:

1. For $\lambda_m L_i > 0$: $F_{1i}(\bar{s} - \bar{s}_{i-1}) = \cos a_i(\bar{s} - \bar{s}_{i-1})$, $\quad F_{2i}(\bar{s} - \bar{s}_{i-1}) = \sin a_i(\bar{s} - \bar{s}_{i-1})$,
2. For $\lambda_m L_i < 0$: $F_{1i}(\bar{s} - \bar{s}_{i-1}) = \cosh a_i(\bar{s} - \bar{s}_{i-1})$, $\quad F_{2i}(\bar{s} - \bar{s}_{i-1}) = \sinh a_i(\bar{s} - \bar{s}_{i-1})$ with $a_i = \sqrt{|\lambda L_i|}$.

The constants A_{1i} and A_{2i} can be determined from the matching conditions:

$$\phi_m(\bar{s}_{i-1}) = \phi_{m,i-1}, \qquad \phi_m'(\bar{s}_{i-1}) = \phi_{m,i-1}' \tag{74}$$

and are given by:

$$A_{1i} = \phi_{m,i-1} - C_{R_m} \frac{N_i}{\lambda_m L_i}, \qquad A_{2i} = \frac{\phi_{m,i-1}'}{a_i}. \tag{75}$$

The quantity $\phi_m(\bar{s}_i) = \phi_{m,i}$ at the right end of the segment is computed along with its derivative as

$$\begin{aligned} \phi_{m,i} &= \phi_{m,i-1} F_{1i}(h) + \frac{\phi_{m,i-1}'}{a_i} F_{2i}(h) + C_{R_m} N_i \frac{[1 - F_{1i}(h)]}{\lambda_m L_i}, \\ \phi_{m,i}' &= \phi_{m,i-1} F_{1i}'(h) + \frac{\phi_{m,i-1}'}{a_i} F_{2i}'(h) - C_{R_m} N_i \frac{F_{1i}'(h)}{\lambda_m L_i}. \end{aligned} \tag{76}$$

The general solution of Eqn. (72) can be constructed using Eqns. (76) and the continuity requirements for ϕ_m and ϕ_m' at the extremities of each integration segment. Since Eqn. (69) is linear, its general solution can be written as a combination of three particular solutions, leveraging the superposition property of linear ODEs:

$$\phi_m(\bar{s}) = c_1 \psi_1(\bar{s}) + c_2 \psi_2(\bar{s}) + C_{R_m} \psi_3(\bar{s}), \tag{77}$$

where c_1 and c_2 are constants. Based on this superposition principle, we can establish the following initial conditions for the particular solutions $\psi_1(\bar{s})$, $\psi_2(\bar{s})$ and $\psi_3(\bar{s})$ of Eqn. (69):

$$\begin{aligned} &\psi_1(0) = 1, \quad \psi_1'(0) = 0, \quad C_{R_m} = 0, \\ &\psi_2(0) = 0, \quad \psi_2'(0) = 1, \quad C_{R_m} = 0, \\ &\psi_3(0) = 0, \quad \psi_3'(0) = 0, \quad C_{R_m} = 1. \end{aligned} \tag{78}$$

The functions $\psi_i(\bar{s}), i = 1, 2, 3$ can be constructed individually using the recurrence relations outlined in Eqn. (76). By applying the boundary conditions, we have

$$\begin{aligned} &\phi_m(0) = 0 \implies c_1 = 0, \\ &\phi_m(1) = 0 \implies c_2 \psi_2(1) + C_{R_m} \psi_3(1) = 0. \end{aligned} \tag{79}$$

Upon substituting Eqn. (77) in Eqn. (71), the constraint can be rewritten as

$$c_2 \int_0^1 \psi_2(\bar{s}) N(\bar{s}) d\bar{s} + C_{R_m} \int_0^1 \psi_3(\bar{s}) N(\bar{s}) d\bar{s} = 0. \tag{80}$$

We construct the following homogeneous system of equations:

$$\begin{bmatrix} \psi_2(1) & \psi_3(1) \\ \int_0^1 \psi_2(\bar{s}) N(\bar{s}) d\bar{s} & \int_0^1 \psi_3(\bar{s}) N(\bar{s}) d\bar{s} \end{bmatrix} \begin{pmatrix} c_2 \\ C_{R_m} \end{pmatrix} = \begin{pmatrix} 0 \\ 0 \end{pmatrix}. \tag{81}$$

For a non-trivial solution to this equation, the determinant,

$$\Delta = \psi_2(1) \int_0^1 \psi_3(\bar{s}) N(\bar{s}) d\bar{s} - \psi_3(1) \int_0^1 \psi_2(\bar{s}) N(\bar{s}) d\bar{s} \tag{82}$$

must be zero. The integrals are evaluated numerically.

We vary the value of λ_m from 0 to 1 and monitor the changes in Δ.

- If there exists at least one value of $\lambda_m \in [0, 1]$ such that $\Delta = 0$, then a non-trivial solution of Eqn. (77) exists that also satisfies the boundary conditions. In this case, the corresponding equilibrium configuration is unstable.
- It no value of $\lambda_m \in [0, 1]$ results in $\Delta = 0$, it implies that only a trivial solution of Eqn. (77) exists. Therefore, the corresponding equilibrium configuration is stable.

6 Results and Discussion

In this section, we begin with the validation of our numerical framework by comparing our results with the well-studied Euler's elastica from existing literature [2]. We consider three canonical boundary conditions, namely, fixed-fixed, pinned-pinned, and fixed-free. Our results are presented as load-displacement curves, also known as equilibrium curves, which have been determined using the continuation algorithm described in Sect. 4.

We use the well-known mathematical analysis tool, AUTO-07p, to validate our numerical results. We then explore solutions for both soft and hard ferromagnetic ribbons under various boundary conditions. A summary of all cases considered is provided in Table 1. For our analysis, we assume that the width of the ferromagnetic ribbon is very small, allowing it to deform into self-intersecting loops while remaining planar. Such self-intersecting loops have been observed in experiments involving elastic ribbons with meticulous longitudinal cuts, as depicted in Fig. 7.

6.1 Euler's Elastica

Figure 8a shows the stability diagram for the first three nonlinear modes of the elastica, which is fixed at one end while the other end remains free. We plot the horizontal displacement of the end-point, $u_3(\bar{s} = 1) = 1 - \int_0^1 \cos\theta(\bar{s}) d\bar{s}$, against the loading parameter $\bar{P}$. Note that $\bar{P} > 0$ corresponds to compressive loads and $\bar{P} < 0$ indicates tensile loads. The solid curves denote stable deformations while the dotted lines represent unstable deformations. We observe that only the first nonlinear mode (mode-1) is stable. This could be attributed to the fact that the energy associated with the first nonlinear mode is the lowest among all modes, as seen in Fig. 8b.

Table 1 Various considered cases in the study

Sections	6.1	6.2	6.3		
Description	Euler's elastica	Case 1 Soft ferromagnet Transverse $\boldsymbol{h}_e$	Case 2: Hard ferromagnet Transverse $\boldsymbol{h}_e$		
			$\boldsymbol{m} = \boldsymbol{t}$		$\boldsymbol{m} = \boldsymbol{n}$
Figures	Fixed-Free (8)	(11)	(8)	but different $\bar{R}$	(14)
	Fixed-Fixed (9)	(12)	(9)	„	(15)
	Pinned-Pinned (10)	(13)	(10)	„	(16)

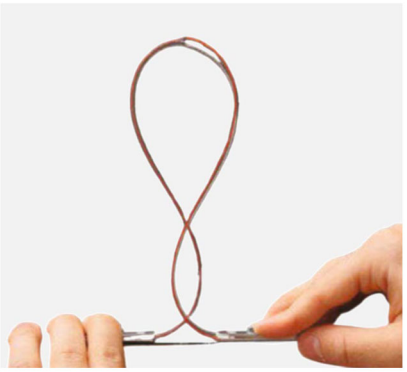


Fig. 7 Experiment conducted by Bigoni et al. [2] showing a self-intersecting Mode-1 deformation of an elastic ribbon subjected to fixed-fixed boundary conditions. The dimensions of the ribbon in the experiment are: $t = 1.5$ mm, $a = 25$ mm and $l = 490$ mm

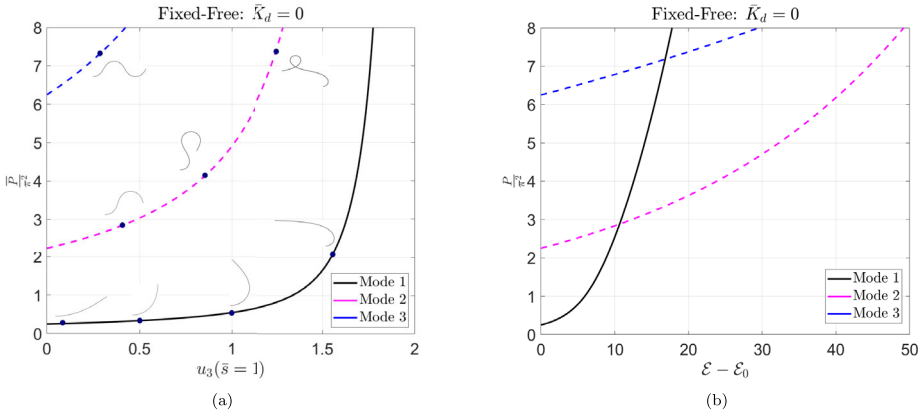


Fig. 8 Euler's elastica: (a) Stability diagram, note that the first critical load is compressive, that is, $\bar{P}_1 = +\frac{\pi^2}{4}$. (b) Total energy curve for fixed-free configuration; $\mathcal{E}_0 = 0$

The stability diagram for the fixed-fixed scenario is shown in Fig. 9a. We observe that the elastica undergoes a primary bifurcation along the first nonlinear mode, which initiates at the first critical $\bar{P}$, as determined from linearized buckling analysis. This bifurcation at the first critical $\bar{P}$ is continuous, as illustrated in Fig. 9b. As $\bar{P}$ is increased beyond the first critical load, the two ends of the ribbon meet. Thereafter, it undergoes snap-through (secondary) bifurcation at $\bar{P} = 10\pi^2$ to the mode-2 branch. At this secondary bifurcation,

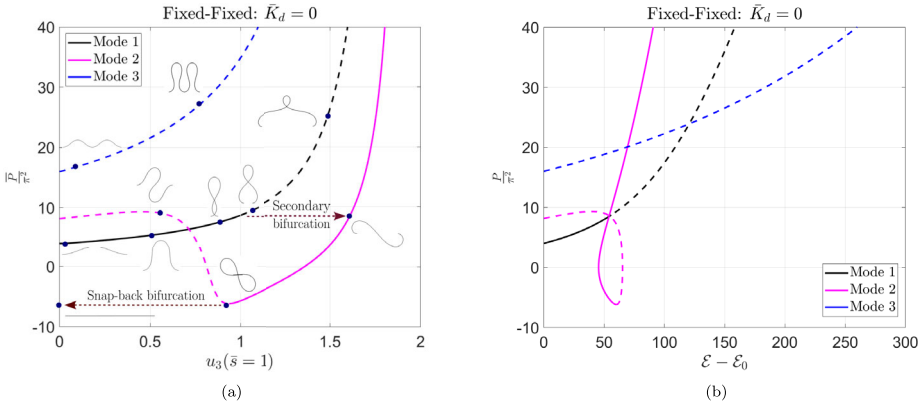


Fig. 9 Euler's elastica: (a) Stability diagram (b) Total energy curve for fixed-fixed configuration; $\mathcal{E}_0 = 0$

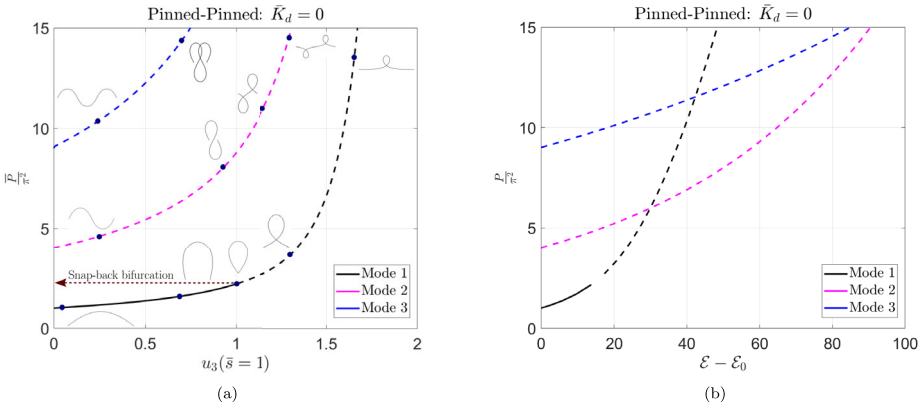


Fig. 10 Euler's elastica: (a) Stability diagram (b) Total energy curve for pinned-pinned configuration; $\mathcal{E}_0 = 0$

the total energy of mode-1 exceeds that of mode-2, as shown in Fig. 9. The ribbon continues to deform on the second mode (mode-2) for $\bar{P} > 10\pi^2$. If $\bar{P}$ is quasi-statically reduced along the mode-2 branch, the nature of buckling load gradually shifts from compressive to tensile until it snap backs to the pre-buckled (reference) tensile configuration at $\bar{P} = -6\pi^2$. The stability diagram for the pinned-pinned case, shown in Fig. 10, indicates that only mode-1 is the stable mode beyond the first critical load. This stability persists until the endpoints meet, after which the ribbon snaps back to its pre-buckled (reference) configuration [15].

A close examination of Eqn. (26) reveals that the equation exhibits reflection symmetry under the transformation $\theta \to -\theta$ if the condition $\bar{R} = 0$ is satisfied. In the pinned-pinned scenario, we find that $\bar{R}$ remains zero for all $\bar{P}_n$ $(n = 1, 2, \dots)$. In constrast, for the fixed-fixed case, $\bar{R} = 0$ for odd values of n $(n = 1, 3, \dots)$ but is non-zero for even n. This change in symmetry could be responsible for the complex bifurcation behaviour observed in Fig. 9a.

6.2 Soft Ferromagnetic Ribbon: Transverse External Magnetic Field, $\bar{h}_e = e_2$

We recall that the demag. energy in the soft magnetic case is given by $K_d at \int (\boldsymbol{e}_2 \cdot \boldsymbol{n})^2 ds$. To minimize this energy, the normal to the centerline tends to align with the $\boldsymbol{e}_3$ direction. This

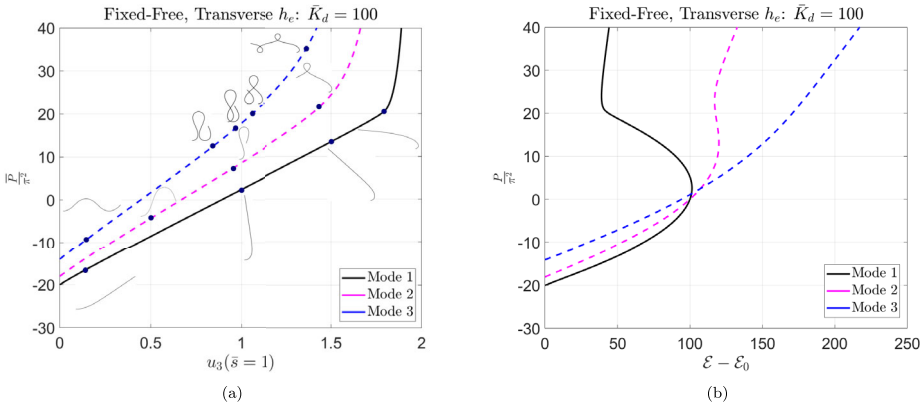


Fig. 11 Soft ferromagnetic ribbon, $\bar{K}_d = 100$: (a) Stability diagram, note that the first critical load is tensile, that is, $\bar{P}_1 = -20.01\pi^2$. (b) Total energy curve for fixed-free configuration under transverse magnetic field; $\mathcal{E}_0 = -100$

alignment promotes the orientation of the ribbon in the $\boldsymbol{e}_2$ direction. We consider $\bar{K}_d = 100$ for our analysis, since the magnetostatic energy becomes comparable to the mechanical energy in this regime.

Figure 11a presents the stability diagram for a fixed-free ferromagnetic ribbon in the presence of a transverse $\boldsymbol{h}_e$ external magnetic field, see Fig. 3. Note that the critical load here is tensile. The first nonlinear mode remains stable for all values of $\bar{P} > -197.53$. This bifurcation is continuous, as demonstrated by the energy plot shown in Fig. 11b.

For the fixed-fixed boundary condition, the soft ferromagnetic ribbon buckles at a tensile load, with mode-1 deformation observed for $\bar{P} > -160.52$, see Fig. 12a. As $\bar{P}$ is increased, the ribbon continues to deform along mode-1. At $\bar{P} \approx 13\pi^2$, the ribbon snaps to the mode-2 branch, as seen in Fig. 12. The ribbon further deforms along the mode-2 branch with a gradual decrease in $\bar{P}$. During unloading, that is, when $\bar{P}$ is decreased along the mode-2 branch, we observe the formation of new stable deformed configurations for tensile loads before the ribbon snaps back to its reference state. We observe a prolonged stretch of a stable segment in the mode-2 branch under the influence of $\boldsymbol{h}_e$ for tensile loads ($\bar{P} < 0$). This stable segment persists even after the two supports have significantly crossed each other. Interestingly, we identify novel and stable states within this segment of the mode-2 branch. This segment is highlighted in Fig. 12a. We have highlighted one such novel and stable deformed configuration in red in Fig. 12a, occurring at an end displacement is $u_3 = 0.65$. It is important to note that this deformed configuration features two self-intersection points. A few intermediate novel deformed configurations are depicted in red in Fig. 12b. Curves exhibiting two self-intersection points are not observed in any stable configuration within the purely elastic case. As $\bar{P}$ is further reduced along this branch, indicating an increase in tensile load, the ribbon undergoes a secondary bifurcation, after which it snaps back to the pre-buckled (reference) tensile configuration.

For the pinned-pinned soft ferromagnetic ribbon, the stability diagram shown in Fig. 13a is qualitatively similar to the purely elastic case. However, in this scenario, the deformed shape aligns along the $\boldsymbol{e}_2$ direction, and the critical load is tensile. Thus, for soft ferromagnetic ribbon across all boundary conditions, the critical load is tensile and can be determined from the linearized equations (Eqn. (24)) about $\theta(\bar{s}) \approx 0$ such that $\sin\theta(\bar{s}) \approx \theta(\bar{s})$

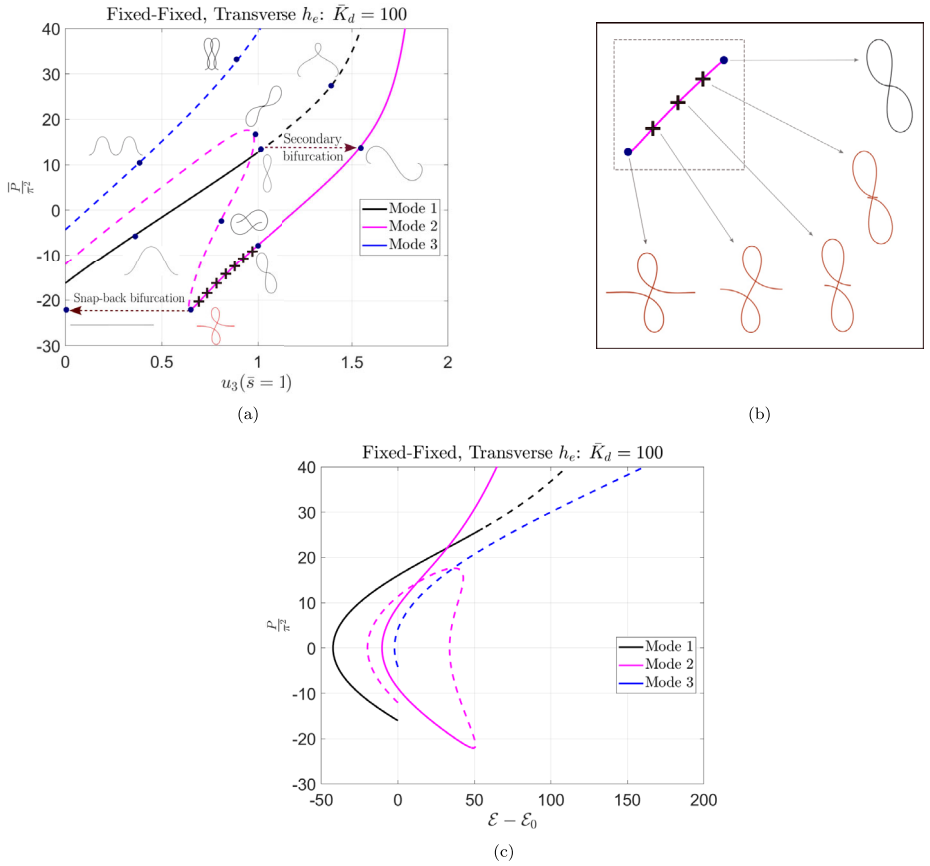


Fig. 12 Soft ferromagnetic ribbon, $\bar{K}_d = 100$: (a) Stability diagram, segment of the mode-2 branch corresponding to novel stable curves is highlighted in '+' symbol. Deformed config. shown in red represents one such novel stable curve on this segment that cannot be observed in purely elastic ribbon. (b) Segment of the mode-2 branch showing novel stable deformed configurations. (c) Total energy curve for fixed-fixed configuration under transverse magnetic field; $\mathcal{E}_0 = -100$

and $\cos\theta(\bar{s}) \approx 1$ as follows:

$$\theta''(\bar{s}) + (\bar{P} + 2\bar{K}_d)\theta(\bar{s}) + \bar{R} = 0, \tag{83}$$

subject to the integral constraint (applicable for fixed-fixed and pinned conditions):

$$\bar{y}(1) = \int_0^1 \theta(\bar{s})\, d\bar{s} = 0.$$

The critical loads for different boundary conditions are given by:

- fixed-free: $\bar{P}_n = \left(n - \frac{1}{2}\right)^2 \pi^2 - 2\bar{K}_d, \quad n = 1, 2, \ldots,$
- fixed-fixed: $\left(2\tan\frac{\sqrt{\bar{P}_n + 2\bar{K}_d}}{2} = \sqrt{\bar{P}_n + 2\bar{K}_d}\right)$; $\bar{P}_1 = 4\pi^2 - 2\bar{K}_d$, $\bar{P}_2 = 8.183\pi^2 - 2\bar{K}_d$, $\bar{P}_3 = 16\pi^2 - 2\bar{K}_d, \ldots,$
- pinned-pinned: $\bar{P}_n = n^2\pi^2 - 2\bar{K}_d$.

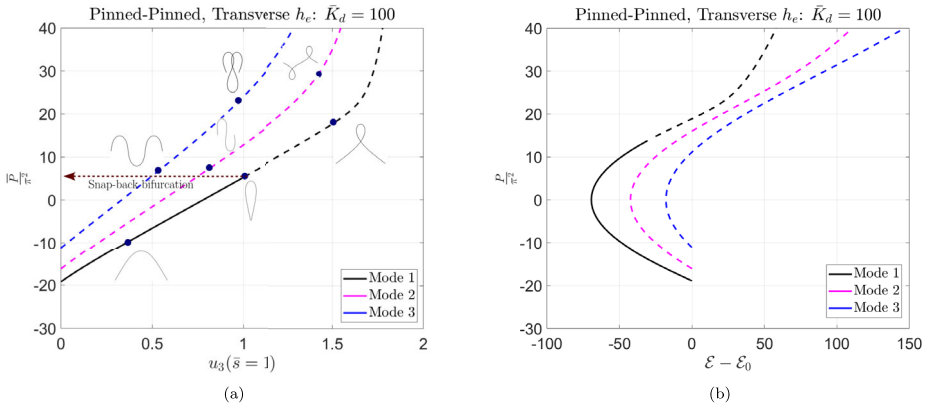


Fig. 13 Soft ferromagnetic ribbon, $\bar{K}_d = 100$: (a) Stability diagram (b) Total energy curve for pinned-pinned configuration under transverse magnetic field; $\mathcal{E}_0 = -100$

6.3 Hard Ferromagnetic Ribbon: Transverse External Magnetic Field, $\bar{\boldsymbol{h}}_e = \pm \boldsymbol{e}_2$

We now present our analysis for the hard ferromagnetic ribbon. Recall that, in this case, the magnetization vector makes a constant angle with the tangent at each point along the curve. A comparison of Eqns. (34) and (26) reveals that the presence of magnetization does not change the structure of Euler's elastica equilibrium equations. For certain combinations of $(\boldsymbol{h}_e, \boldsymbol{m}(\bar{s}))$, the deformed configurations corresponding to the hard magnetic case can be derived by simply translating the stability curves of Euler's elastica (Figs. 8, 9, 10) along the $\bar{P}$-axis, as depicted in Figs. 14, 15 and 16. In other cases, the stability curves for the hard magnetic case remain identical to those of Euler's elastica. For the former combinations of $(\boldsymbol{h}_e, \boldsymbol{m}(\bar{s}))$, the critical loads are either significantly higher or lower than those corresponding to the classical elastica. This difference can be observed by linearizing Eqn. $(34)_2$.

Our proposed model and results matches with the equilibrium equation for the planar deformation of a hard ferromagnetic ribbon under fixed-free configuration, as reported by Zhao et al [32] and Wang et al. [30, 31], when subjected to an external magnetic field without any mechanical load.

Case of $\boldsymbol{m}(\bar{s}) = \boldsymbol{t}(\bar{s})$: We compare the equilibrium equation of the hard ferromagnetic ribbon with $\boldsymbol{m}(\bar{s}) = \boldsymbol{t}(\bar{s})$ (Eqn. $(34)_1$) and Eqn. (26) and make the following observations:

- The critical buckling load remains unaffected.
- The reactions Q and R_e are related by the equation

$$\bar{Q} = \bar{R}_e \mp 2\bar{K}_d h_e \tag{84}$$

when $\boldsymbol{h}_e = \pm h_e \boldsymbol{e}_2$.

The stability curves in this scenario are identical to those of the classical elastica.

Case of $\boldsymbol{m}(\bar{s}) = \boldsymbol{n}(\bar{s})$: The stability curves of the hard ferromagnetic ribbon with normal magnetization distribution, $\boldsymbol{m}(\bar{s}) = \boldsymbol{n}(\bar{s})$, are obtained by translating those of Euler's elastica along the $\bar{P}$ axis, with the measure of translation being proportional to h_e. Figures 14, 15 and 16 show these stability curves, considering $\bar{K}_d h_e = 100$.

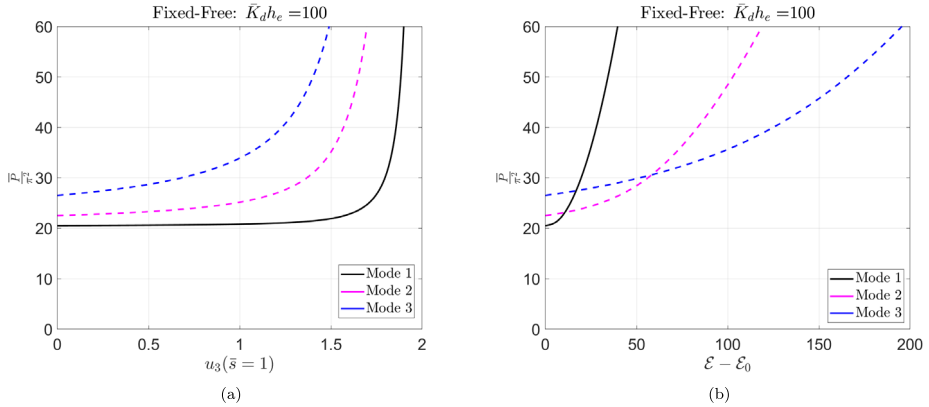


Fig. 14 Hard ferromagnetic ribbon: Axial h_e, Fixed-Free, $\boldsymbol{m}=\boldsymbol{t}(\bar{s})$, $\bar{K}_d h_e = 100$: (a) Stability diagram (b) Total energy curve; $\mathcal{E}_0 = 0$

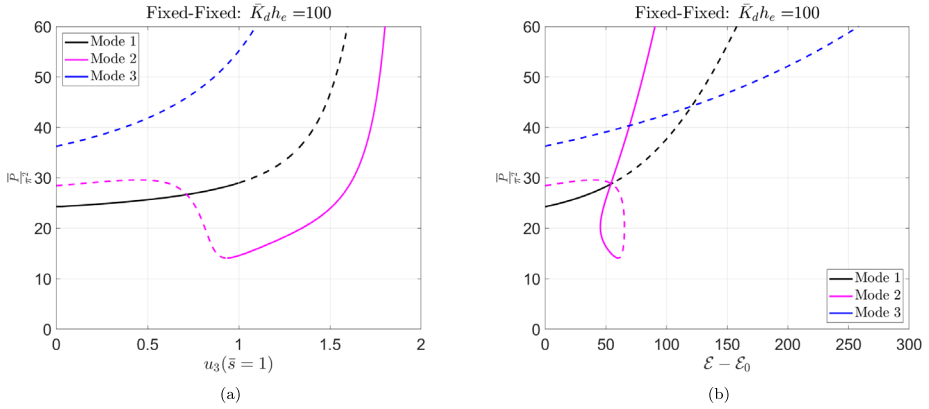


Fig. 15 Hard ferromagnetic ribbon: Axial h_e, Fixed-Fixed, $\boldsymbol{m}=\boldsymbol{t}(\bar{s})$, $\bar{K}_d h_e = 100$: (a) Stability diagram (b) Total energy curve; $\mathcal{E}_0 = 0$

In the case where $\boldsymbol{h}_e = h_e \boldsymbol{e}_2$, the critical load significantly exceeds that of the classical elastica, as evident from Eqns. $(34)_2$ and (26). On the other hand, the critical load becomes much lower when $\boldsymbol{h}_e = -h_e \boldsymbol{e}_2$. The reactions are related by:

$$\bar{Q} = \bar{R}_e. \tag{85}$$

6.4 Limit as $(\bar{K}_a \to 0$ and $\bar{K}_d \to \infty)$ or $\left(K_a a t \ll \frac{EI}{l} \ll K_d a t\right)$

In this section, we explore the deformation of our planar ferromagnetic ribbons in the limit as $\bar{K}_a \to 0$ and $\bar{K}_d \to \infty$. This limit is also attained for a soft ferromagnetic ribbon ($K_a \approx 0$) with E, a, l, and K_d are held constant, and as $t \to 0$. This represents a physically relevant scenario for soft ferromagnetic nano rods/ribbons utilized in MEMS devices [24].

As $\bar{K}_d \to \infty$, the magnetostatic energy is much larger than the elastic energy. In this regime, the magnetisation $\boldsymbol{m}$ and the normal $\boldsymbol{n}$ are perpendicular almost all along the length

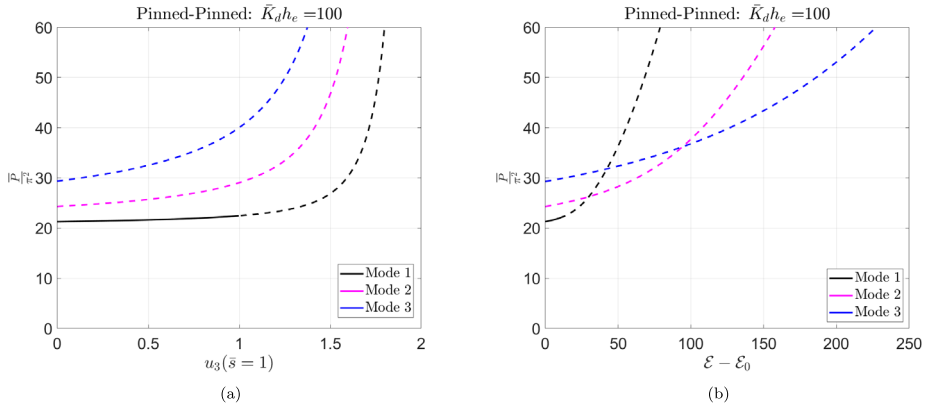


Fig. 16 Hard ferromagnetic ribbon: Axial h_e, Pinned-Pinned, $\boldsymbol{m} = \boldsymbol{t}(\bar{s})$, $\bar{K}_d h_e = 100$: (a) Stability diagram (b) Total energy curve; $\mathcal{E}_0 = 0$

of the ribbon, except in short intervals where this condition cannot be satisfied due to either the imposed mechanical boundary conditions or the isoperimetric constraint arising from inextensibility. These short intervals exhibit curvature, characterized by a radius denoted as r_c, as shown in Fig. 17. An estimate for $r_c = (\kappa_c^{-1})$ can be obtained by balancing the elastic energy and demagnetisation energy, as outlined below:

$$\text{Total energy}: \quad \frac{EI}{2}\int_0^l \kappa^2(s)ds + K_d a t \int_0^l (\boldsymbol{m}\cdot\boldsymbol{n})^2 ds \approx EI\int_0^{2\pi r}\frac{1}{r^2}ds + K_d a t\int_0^{2\pi r} ds \\ = \frac{EI\cdot 2\pi}{r} + K_d a t\cdot 2\pi r. \tag{86}$$

By optimising the total energy with respect to r, we obtain $r_c \sim \mathcal{O}\left(t\sqrt{\frac{E}{K_d}}\right)$. The deformed configurations in this regime for fixed-free, fixed-fixed, and pinned-pinned soft ferromagnetic ribbons are shown in Fig. 17.

A similar analysis for a hard ferromagnetic ribbon indicates that the radius of curvature, r_c, is approximately on the order of $\mathcal{O}\left(t\sqrt{\frac{E}{K_d h_e}}\right)$. This implies that the radius of curvature decreases as the external magnetic field is increased in the case of a hard ferromagnetic ribbon.

7 Conclusions

In this paper, we have presented a novel model that combines ideas from Euler's elastica and continuum theory of micromagnetics to predict the deformation of ferromagnetic ribbons. We have analysed the buckling of a planar inextensible ribbon subjected to a large but constant external magnetic field and a gradually applied quasi-static load. While maintaining fixed magnetisation, we investigate the influence of magnetisation on the deformation of the planar ferromagnetic ribbon. Exploring how deformation influences magnetisation is an area for future research, although it presents a challenging problem. Our analysis commences by deriving and incorporating the magnetostatic energy of a curved structure into

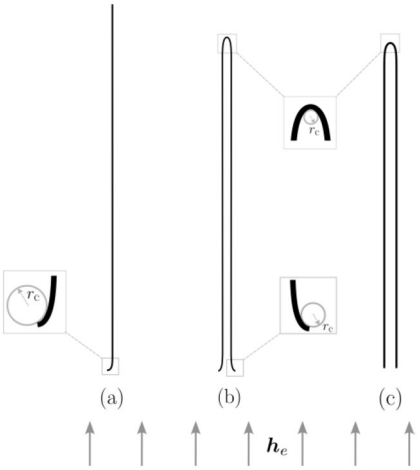


Fig. 17 Deformed shapes of soft ferromagnetic ribbon for $\bar{K}_d = 10^4$ showing osculating circles at the curved bends: (a) fixed-free (b) fixed-fixed, and (c) pinned-pinned cases. The respective values of $(\bar{P}, u_3(\bar{s}=1))$ are $(0.4\pi^2, 0.99)$, $(6\pi^2, 0.96)$ and $(2\pi^2, 0.98)$

the total energy of the system. We derive the equilibrium equations and solve them numerically to obtain the equilibrium path as the load is varied. Further, we also determine the stability of the equilibrium solutions by casting the second variation of the total energy as a Sturm-Liouville eigenvalue problem, which is solved numerically.

We examine ribbons composed of both hard and soft ferromagnetic properties, under a transversely applied external magnetic field and various mechanical boundary conditions. We observe that the critical buckling load is tensile mainly for a soft ferromagnetic ribbon under various canonical boundary conditions. Interestingly, our findings reveal the presence of novel stable configurations in the case of a fixed-fixed setup with a transversally applied external magnetic field. We anticipate that these stable configurations can be observed through meticulously conducted experiments.

Our model is applicable within specific parameter ranges. For a typical ferromagnetic material such as iron (Fe) or nickel (Ni), the Young's modulus (E) and the magnetostatic energy density (K_d) are approximately $E \sim 10^{11}$ and $K_d \sim 10^5$, respectively. The aspect ratio, defined as the ratio of the width (a) to the thickness (t), can be determined by ensuring that $\bar{\kappa} \ll 1$, yielding ${}^{a}/_{t} \sim \mathcal{O}(10^1)$. The ratio of the thickness to the length of the ribbon is determined by the values of $\bar{K}_d$ derived from the conducted simulations. Our simulations reveal that in soft ferromagnets, the magnetic effect becomes significant when $\bar{K}_d \sim 100$. Hence, ${}^{l}/_{t} \sim 10\sqrt{{}^{E}/_{K_d}}$. Similarly, for hard ferromagnets, magnetic effects are observed when $\bar{K}_d h_e \sim 100$, resulting in: ${}^{l}/_{t} \sim 10\sqrt{{}^{E}/_{K_d h_e}}$. Furthermore, for a hard ferromagnet, the maximum external magnetic field is determined by ensuring the exchange energy remains non-negative, expressed as $\kappa_c < \kappa_{\max} = {}^{2}/_{t}$, consequently leading to a maximum external magnetic field $h_e < \sqrt{{}^{E}/_{K_d}}$.

Our analysis can be readily extended to understanding the deformation of planar ferromagnetic rods. The magnetostatic energy of planar ferromagnetic rod scales as $\mathcal{O}(K_d \pi r^2 l)$ [28]. A balance of the elastic energy $\mathcal{O}(E\pi\left(\frac{r^4}{8l}\right))$, and the magnetostatic energy for ferromagnetic rods would suggest that our analysis remains valid for rods with an aspect ratio of $\mathcal{O}\left(\sqrt{\frac{E}{8Kd}}\right)$.

The stability analysis conducted in our study solely examines planar perturbations. It is widely recognized that, in the case of Euler's elastica, stability under planar perturbations does not guarantee stability of the equilibrium configurations under fully three-dimensional

perturbations [17]. Motivated by this study, we outline the following future research directions:

- Explore stability under three-dimensional perturbations, and ascertain the potential role of the vertical reaction, $\bar{R}$, in this analysis.
- Investigating the influence of twist and out-of-plane deformation on ferromagnetic ribbons.
- Design laboratory experiments to observe novel stable deformed configurations of ferromagnetic ribbon structures, as identified in our analysis.

Appendix A: Derivation of Magnetostatic Energy

In this section, we present the calculation of the leading order demag. energy of a deformed planar ferromagnetic ribbon. The magnetostatic energy is evaluated by solving Maxwell's equations of magnetostatics

$$\begin{aligned} \nabla \times \boldsymbol{h}_m(\boldsymbol{x}) &= 0, \\ \nabla \cdot (\boldsymbol{h}_m + \boldsymbol{m}(\boldsymbol{x})) &= 0. \end{aligned} \tag{87}$$

Applying Fourier transform to the above equations imply

$$\boldsymbol{\xi} \times \hat{\boldsymbol{h}}_m = 0, \tag{88}$$

$$\boldsymbol{\xi} \cdot (\hat{\boldsymbol{h}}_m + \hat{\boldsymbol{m}}) = 0, \tag{89}$$

where $\hat{\boldsymbol{f}}(\boldsymbol{\xi}) := \int_{\mathbb{R}^3} \boldsymbol{f}(\boldsymbol{x}) \exp(-i2\pi \boldsymbol{x} \cdot \boldsymbol{\xi}) d\boldsymbol{x}$. Eqn. (88) implies $\hat{\boldsymbol{h}}_m \parallel \boldsymbol{\xi}$ and hence,

$$\hat{\boldsymbol{h}}_m = (\hat{\boldsymbol{h}}_m \cdot \hat{\boldsymbol{\xi}})\hat{\boldsymbol{\xi}} \text{ where } \hat{\boldsymbol{\xi}} = \frac{\boldsymbol{\xi}}{|\boldsymbol{\xi}|}. \tag{90}$$

Eqn. (89) implies that $\boldsymbol{\xi} \cdot \hat{\boldsymbol{h}}_m = -\boldsymbol{\xi} \cdot \hat{\boldsymbol{m}}$ and hence $\hat{\boldsymbol{h}}_m = -(\hat{\boldsymbol{\xi}} \cdot \hat{\boldsymbol{m}})\hat{\boldsymbol{\xi}}$. Using Planchevel's identity, we can then write the magnetostatic energy as follows

$$\int_{\mathbb{R}^3} |\boldsymbol{h}_m|^2 d\boldsymbol{x} = \int_{\mathbb{R}^3} \left|\hat{\boldsymbol{h}}_m\right|^2 d\boldsymbol{\xi} = \int_{\mathbb{R}^3} (\hat{\boldsymbol{\xi}} \cdot \hat{\boldsymbol{m}})^2 d\boldsymbol{\xi} = \int_{\mathbb{R}^3} \frac{(\boldsymbol{\xi} \cdot \hat{\boldsymbol{m}})^2}{|\boldsymbol{\xi}|^2} d\boldsymbol{\xi} = \int_{\mathbb{R}^3} \frac{\left|\widehat{\nabla \cdot \boldsymbol{m}}\right|^2}{|\boldsymbol{\xi}|^2} d\boldsymbol{\xi}. \tag{91}$$

We carry out the above integration in the material frame $(\boldsymbol{d}_1(s), \boldsymbol{d}_2(s), \boldsymbol{d}_3(s))$ and $\boldsymbol{x} : (s, \tilde{a}, \tilde{t}) \mapsto \boldsymbol{r}(s) + \tilde{a}\boldsymbol{d}_1(s) + \tilde{t}\boldsymbol{d}_2(s)$. The Fourier transform in the material frame is given as follows:

$$\begin{aligned} \mathcal{F}[\nabla \cdot \boldsymbol{m}](\boldsymbol{\xi}) = \widehat{\nabla \cdot \boldsymbol{m}}(\boldsymbol{\xi}) &= \int_{\Omega} (\nabla \cdot \boldsymbol{m}) \exp(-i2\pi \boldsymbol{x} \cdot \boldsymbol{\xi}) d\boldsymbol{x} \\ &= \int_{\Omega} (\nabla \cdot \boldsymbol{m}) \exp\big(-i2\pi (\boldsymbol{r}(s) + \tilde{a}\boldsymbol{d}_1(s) + \tilde{t}\boldsymbol{d}_2(s)) \cdot \boldsymbol{\xi}\big) J ds d\tilde{t} d\tilde{a}, \end{aligned} \tag{92}$$

here, $\mathcal{F}(v)$ denotes Fourier transform of v and $J = \left|\frac{\partial(x_1, x_2, x_3)}{\partial(s, \tilde{a}, \tilde{t})}\right|$ is the Jacobian associated with the change of variables. The divergence of $\boldsymbol{m}$ is invariant upon coordinate transformation and is expressed as follows in the material frame:

$$\nabla \cdot \boldsymbol{m} = \frac{1}{h_s h_{\tilde{a}} h_{\tilde{t}}} \left\{ \frac{\partial(h_{\tilde{a}} h_{\tilde{t}} m_{d_3})}{\partial s} + \frac{\partial(h_{\tilde{t}} h_s m_{d_1})}{\partial \tilde{a}} + \frac{\partial(h_s h_{\tilde{a}} m_{d_2})}{\partial \tilde{t}} \right\}, \tag{93}$$

here, $h_s = \left|\frac{\partial \boldsymbol{x}}{\partial s}\right|$, $h_{\tilde{a}} = \left|\frac{\partial \boldsymbol{x}}{\partial \tilde{a}}\right|$ and $h_{\tilde{t}} = \left|\frac{\partial \boldsymbol{x}}{\partial \tilde{t}}\right|$.

Note:

- $\frac{\partial \boldsymbol{x}}{\partial s} = \boldsymbol{r}'(s) + \tilde{a}\boldsymbol{d}_1'(s) + \tilde{t}\boldsymbol{d}_2'(s) = \boldsymbol{d}_3(s) + \tilde{t}\kappa\boldsymbol{d}_3(s) = (1+\tilde{t}\kappa)\boldsymbol{d}_3(s) \implies h_s = (1+\tilde{t}\kappa)$,
- $\frac{\partial \boldsymbol{x}}{\partial \tilde{a}} = \boldsymbol{d}_1(s) \implies h_{\tilde{a}} = 1$,
- $\frac{\partial \boldsymbol{x}}{\partial \tilde{t}} = \boldsymbol{d}_2(s) \implies h_{\tilde{t}} = 1$.

Furthermore, $J = h_s h_{\tilde{a}} h_{\tilde{t}}$, and hence

$$\begin{aligned}\nabla \cdot \boldsymbol{m} &= \frac{1}{J}\left\{\frac{\partial m_{d_3}}{\partial s} + (1+\tilde{t}\kappa)\frac{\partial m_{d_1}}{\partial \tilde{a}} + (1+\tilde{t}\kappa)\frac{\partial m_{d_2}}{\partial \tilde{t}} + \kappa m_{d_2}\right\} \\ &= \frac{1}{J}\left\{(\partial_{\tilde{a}} m_{d_1} + \partial_{\tilde{t}} m_{d_2} + \partial_s m_{d_3}) + \kappa(\tilde{t}\partial_{\tilde{a}} m_{d_1} + \tilde{t}\partial_{\tilde{t}} m_{d_2} + m_{d_2})\right\}. \end{aligned} \tag{94}$$

Substituting the above expression for $\nabla \cdot \boldsymbol{m}$ in Eqn. (92) can now be written as follows:

$$\begin{aligned}\mathcal{F}[\nabla \cdot \boldsymbol{m}](\boldsymbol{\xi}) = \int_\Omega \frac{1}{J}&\left\{(\partial_{\tilde{a}} m_{d_1} + \partial_{\tilde{t}} m_{d_2} + \partial_s m_{d_3}) + \kappa(\tilde{t}\partial_{\tilde{a}} m_{d_1} + \tilde{t}\partial_{\tilde{t}} m_{d_2} + m_{d_2})\right\} \\ &\times \exp\big(-i2\pi(\boldsymbol{r}(s) + \tilde{a}\boldsymbol{d}_1(s) + \tilde{t}\boldsymbol{d}_2(s))\cdot\boldsymbol{\xi}\big) J\, ds\, d\tilde{t}\, d\tilde{a}. \end{aligned} \tag{95}$$

Since $\boldsymbol{r}(0) = \boldsymbol{0}$ and $\boldsymbol{r}(s)\cdot\boldsymbol{\xi} = \int_0^s \boldsymbol{d}_3(s')ds'\cdot\boldsymbol{\xi} = s\xi_{d_3}$ and therefore, $(\boldsymbol{r}(s) + \tilde{a}\boldsymbol{d}_1(s) + \tilde{t}\boldsymbol{d}_2(s))\cdot\boldsymbol{\xi} = \tilde{a}\xi_{d_1} + \tilde{t}\xi_{d_2} + s\xi_{d_3}$. The divergence of $\boldsymbol{m}$ in the material frame is written as a sum of these six integrals:

$$\mathcal{F}[\nabla \cdot \boldsymbol{m}](\boldsymbol{\xi}) = I_1 + I_2 + I_3 + I_4 + I_5 + I_6, \tag{96}$$

where

$$\begin{aligned}
I_1 &= \mathcal{F}[\partial_{\tilde{a}} m_{d_1}](\boldsymbol{\xi}_d) = \xi_{d_1} F_0(a,\xi_{d_1}) F_0(t,\xi_{d_2}) \mathcal{F}[m_{d_1}\chi_{(0,l)}(s)](\xi_{d_3}) \quad \text{(even in } \xi_{d_2}\text{)}, \\
I_2 &= \mathcal{F}[\partial_{\tilde{t}} m_{d_2}](\boldsymbol{\xi}_d) = \xi_{d_2} F_0(a,\xi_{d_1}) F_0(t,\xi_{d_2}) \mathcal{F}[m_{d_2}\chi_{(0,l)}(s)](\xi_{d_3}) \quad \text{(odd in } \xi_{d_2}\text{)}, \\
I_3 &= \mathcal{F}[\partial_s m_{d_3}](\boldsymbol{\xi}_d) = F_0(a,\xi_{d_1}) F_0(t,\xi_{d_2}) \mathcal{F}[\partial_s m_{d_3}\chi_{(0,l)}(s)](\xi_{d_3}) \quad \text{(even in } \xi_{d_2}\text{)}, \\
I_4 &= \mathcal{F}[\kappa\tilde{t}\partial_{\tilde{a}} m_{d_1}](\boldsymbol{\xi}_d) = \xi_{d_1} F_0(a,\xi_{d_1}) F_1(t,\xi_{d_2}) \mathcal{F}[\kappa m_{d_1}\chi_{(0,l)}(s)](\xi_{d_3}) \quad \text{(odd in } \xi_{d_2}\text{)}, \\
I_5 &= \mathcal{F}[\kappa\tilde{t}\partial_{\tilde{t}} m_{d_2}](\boldsymbol{\xi}_d) = F_0(a,\xi_{d_1}) \xi_{d_2} F_1(t,\xi_{d_2}) \mathcal{F}[\kappa m_{d_2}\chi_{(0,l)}(s)](\xi_{d_3}) \quad \text{(even in } \xi_{d_2}\text{)}, \\
I_6 &= \mathcal{F}[\kappa m_{d_2}](\boldsymbol{\xi}_d) = F_0(a,\xi_{d_1}) F_1(t,\xi_{d_2}) \mathcal{F}[\kappa m_{d_2}\chi_{(0,l)}(s)](\xi_{d_3}) \quad \text{(even in } \xi_{d_2}\text{)},
\end{aligned} \tag{97}$$

where $F_0(v,\eta)$ and $F_1(v,\eta)$ are defined as follows:

$$F_0(v,\eta) = \int_{-v/2}^{v/2} \exp\big(-i2\pi\eta v'\big)dv' \quad \text{and} \quad F_1(v,\eta) = \int_{-v/2}^{v/2} v' \exp\big(-i2\pi\eta v'\big)dv'.$$

The magnetostatic energy can now be expressed in terms of I_1, I_2, I_3, I_4, I_5, I_6 as follows:

$$\begin{aligned}\int_{\mathbb{R}^3} \frac{\left|\widehat{\nabla\cdot\boldsymbol{m}}(\boldsymbol{\xi}_d)\right|^2}{\left|\boldsymbol{\xi}_d\right|^2} d\boldsymbol{\xi}_d &= \int_{\mathbb{R}^3} \frac{(I_1+I_2+I_3+I_4+I_5+I_6)^2}{\left|\boldsymbol{\xi}_d\right|^2} \\ &= \underbrace{\int \frac{I_1^2}{\left|\boldsymbol{\xi}_d\right|^2}}_{\mathcal{O}(t^2)} + \underbrace{\int \frac{I_2^2}{\left|\boldsymbol{\xi}_d\right|^2}}_{\mathcal{O}(t)} + \underbrace{\int \frac{I_3^2}{\left|\boldsymbol{\xi}_d\right|^2}}_{\mathcal{O}(t^2)} + \underbrace{\int \frac{I_4^2}{\left|\boldsymbol{\xi}_d\right|^2}}_{\mathcal{O}(t^5)} + \underbrace{\int \frac{I_5^2}{\left|\boldsymbol{\xi}_d\right|^2}}_{\mathcal{O}(t^3)} + \underbrace{\int \frac{I_6^2}{\left|\boldsymbol{\xi}_d\right|^2}}_{\mathcal{O}(t^3)}\end{aligned}$$

$$+\underbrace{2\int \frac{I_1 I_3}{|\boldsymbol{\xi}_d|^2}}_{\mathcal{O}(t^2)}+\underbrace{2\int \frac{I_1 I_5}{|\boldsymbol{\xi}_d|^2}}_{\mathcal{O}(t^3)}+\underbrace{2\int \frac{I_1 I_6}{|\boldsymbol{\xi}_d|^2}}_{\mathcal{O}(t^2)}+\underbrace{2\int \frac{I_2 I_4}{|\boldsymbol{\xi}_d|^2}}_{\mathcal{O}(t^3)}+\underbrace{2\int \frac{I_3 I_5}{|\boldsymbol{\xi}_d|^2}}_{\mathcal{O}(t^3)}+\underbrace{2\int \frac{I_3 I_6}{|\boldsymbol{\xi}_d|^2}}_{\mathcal{O}(t^2)}+\underbrace{2\int \frac{I_5 I_6}{|\boldsymbol{\xi}_d|^2}}_{\mathcal{O}(t^3)}. \tag{98}$$

The remaining product terms are odd functions in ξ_{d_2} and hence they integrate out to zero. Therefore we have the leading order term for the magnetostatic energy as follows:

$$\int_{\mathbb{R}^3} \frac{\left|\widehat{\nabla\cdot\boldsymbol{m}}(\boldsymbol{\xi}_d)\right|^2}{|\boldsymbol{\xi}_d|^2} d\boldsymbol{\xi}_d = \int_{\mathbb{R}^3} \frac{I_2^2}{|\boldsymbol{\xi}_d|^2} d\boldsymbol{\xi}_d + \mathcal{O}(t^2). \tag{99}$$

Now,

$$\lim_{t\to 0}\int_{\mathbb{R}^3} \frac{I_2^2}{|\boldsymbol{\xi}_d|^2} d\boldsymbol{\xi}_d = at\int_{\mathbb{R}} \left|\widehat{m_{d_2}}(\xi_{d_3})\right|^2 d\xi_{d_3} + \mathcal{O}(t^2) = at\int_{s=0}^{l} (m_{d_2})^2 ds + \mathcal{O}(t^2). \tag{100}$$

Hence, we have

$$\int_{\mathbb{R}^3} |\boldsymbol{h}_m|^2 d\boldsymbol{x} = at\int_{s=0}^{l} (m_{d_2})^2 ds + \mathcal{O}(t^2). \tag{101}$$

Note that for a flat planar ribbon $\boldsymbol{d}_3(s) = \boldsymbol{e}_3$ and $\boldsymbol{d}_2(s) = \boldsymbol{e}_2$. Under these conditions, the leading-order magnetostatic energy term derived in the above expression reduces to the form reported in [7, 12].

Appendix B: Derivation of Exchange Energy

The centerline representation is given by

$$\boldsymbol{x}(s,\tilde{a},\tilde{t}) = \boldsymbol{r}(s) + \tilde{a}\boldsymbol{d}_1(s) + \tilde{t}\boldsymbol{d}_2(s). \tag{102}$$

We define $\{\boldsymbol{g}_a, \boldsymbol{g}_t, \boldsymbol{g}_s\}$ is the natural basis for the mapping defined in Eqn. (102), are expressed as

$$\boldsymbol{g}_a(s) = \frac{\partial \boldsymbol{x}}{\partial \tilde{a}}, \qquad \boldsymbol{g}_t(s) = \frac{\partial \boldsymbol{x}}{\partial \tilde{t}}, \qquad \boldsymbol{g}_s(s) = \frac{\partial \boldsymbol{x}}{\partial s}. \tag{103}$$

Evidently, the basis $\{\boldsymbol{g}_a, \boldsymbol{g}_t, \boldsymbol{g}_s\}$ is orthogonal but not orthonormal. Let $\{\boldsymbol{g}^a, \boldsymbol{g}^t, \boldsymbol{g}^s\}$ be the reciprocal basis, that is, $\boldsymbol{g}^i \cdot \boldsymbol{g}_j = \delta^i_j$, $i, j \in \{a, t, s\}$. We express the magnetisation vector as

$$\boldsymbol{m} = m^a \boldsymbol{g}_a + m^t \boldsymbol{g}_t + m^s \boldsymbol{g}_s, \text{ where } m^i = \boldsymbol{m}\cdot\boldsymbol{g}^i \ (i = 1, 2, 3), \tag{104}$$

and its gradient as $\nabla\boldsymbol{m} = \nabla_i m^k \boldsymbol{g}_k \otimes \boldsymbol{g}^i$, here, $\nabla_i m^k$ are the covariant derivatives of $\boldsymbol{m}$. Now, $\nabla_i m^k = \left(m^k_{,i} + \Gamma^k_{ij} m^j\right)$, where Γ^k_{ij} are the Christoffel symbols, and is given by $\Gamma^k_{ij} := \boldsymbol{g}^k \cdot \boldsymbol{g}_{i,j}$. Out of the 27 Christoffel symbols, only the following three are non-zero:

$$\begin{aligned}
\Gamma^s_{ts} &= \boldsymbol{g}^s \cdot \boldsymbol{g}_{t,s} = \frac{\boldsymbol{d}_3(s)}{(1+\kappa t)} \cdot \boldsymbol{g}_{t,s} = \frac{\boldsymbol{d}_3 \cdot \boldsymbol{d}_2'(s)}{1+\kappa t} = \kappa \frac{\boldsymbol{d}_3(s)\cdot\boldsymbol{d}_3(s)}{(1+\kappa t)} = \frac{\kappa}{(1+\kappa\tilde{t})} = \Gamma^s_{st}, \\
\Gamma^t_{ss} &= \boldsymbol{g}^t \cdot \boldsymbol{g}_{s,s} = \boldsymbol{d}_2(s)\cdot(1+\kappa\tilde{t})\boldsymbol{d}_3'(s) = -\kappa(1+\kappa\tilde{t})\boldsymbol{d}_2(s)\cdot\boldsymbol{d}_2(s) = -\kappa(1+\kappa\tilde{t}).
\end{aligned} \tag{105}$$

Hence,

$$\begin{aligned}\nabla \boldsymbol{m} = &\left(\frac{\partial m^a}{\partial \tilde{a}}\right)\boldsymbol{g}_a\boldsymbol{g}^a + \left(\frac{\partial m^a}{\partial \tilde{t}}\right)\boldsymbol{g}_a\boldsymbol{g}^t + \left(\frac{\partial m^a}{\partial s}\right)\boldsymbol{g}_a\boldsymbol{g}^s \\ &+ \left(\frac{\partial m^t}{\partial \tilde{a}}\right)\boldsymbol{g}_t\boldsymbol{g}^a + \left(\frac{\partial m^t}{\partial \tilde{t}}\right)\boldsymbol{g}_t\boldsymbol{g}^t + \left(\frac{\partial m^t}{\partial s} - \kappa(1+\kappa t)m^s\right)\boldsymbol{g}_t\boldsymbol{g}^s \\ &+ \left(\frac{\partial m^s}{\partial \tilde{a}}\right)\boldsymbol{g}_s\boldsymbol{g}^a + \left(\frac{\partial m^s}{\partial \tilde{t}} + \frac{\kappa}{(1+\kappa\tilde{t})}m^s\right)\boldsymbol{g}_s\boldsymbol{g}^t + \left(\frac{\partial m^s}{\partial s} + \frac{\kappa m^t}{(1+\kappa\tilde{t})}\right)\boldsymbol{g}_s\boldsymbol{g}^s.\end{aligned} \tag{106}$$

We can write the above expression in terms of orthonormal basis of $(\boldsymbol{d}_1, \boldsymbol{d}_2, \boldsymbol{d}_3)$ using the physical components of $\boldsymbol{m}$, that is, $(m_{d_1}, m_{d_2}, m_{d_3})$ as follows:

$$\begin{aligned}\nabla \boldsymbol{m} = &\left(\frac{\partial m_{d_1}}{\partial \tilde{a}}\right)\boldsymbol{d}_1\otimes\boldsymbol{d}_1 + \left(\frac{\partial m_{d_1}}{\partial \tilde{t}}\right)\boldsymbol{d}_1\otimes\boldsymbol{d}_2 + \frac{1}{(1+\kappa\tilde{t})}\frac{\partial m_{d_1}}{\partial s}\boldsymbol{d}_1\otimes\boldsymbol{d}_3 \\ &+ \left(\frac{\partial m_{d_2}}{\partial \tilde{a}}\right)\boldsymbol{d}_2\otimes\boldsymbol{d}_1 + \left(\frac{\partial m_{d_2}}{\partial \tilde{t}}\right)\boldsymbol{d}_2\otimes\boldsymbol{d}_2 + \frac{1}{(1+\kappa\tilde{t})}\left(\frac{\partial m_{d_2}}{\partial s} - \kappa m_{d_3}\right)\boldsymbol{d}_2\otimes\boldsymbol{d}_3 \\ &+ \left(\frac{\partial m_{d_3}}{\partial \tilde{a}}\right)\boldsymbol{d}_3\otimes\boldsymbol{d}_1 + \left(\frac{\partial m_{d_3}}{\partial \tilde{t}}\right)\boldsymbol{d}_3\otimes\boldsymbol{d}_2 + \frac{1}{(1+\kappa\tilde{t})}\left(\frac{\partial m_{d_3}}{\partial s} + \kappa m_{d_2}\right)\boldsymbol{d}_3\otimes\boldsymbol{d}_3,\end{aligned} \tag{107}$$

where $\boldsymbol{g}^s = \frac{1}{(1+\kappa\tilde{t})}\boldsymbol{d}_3(s)$, $\boldsymbol{g}_s = \left(1+\kappa\tilde{t}\right)\boldsymbol{d}_3(s)$. We note that $m_{d_1} = \boldsymbol{m}\cdot\boldsymbol{d}_1(s) = \boldsymbol{m}\cdot\boldsymbol{g}^a$, $m_{d_2} = \boldsymbol{m}\cdot\boldsymbol{d}_2(s) = \boldsymbol{m}\cdot\boldsymbol{g}^t = m^t$, $m_{d_3} = \boldsymbol{m}\cdot\boldsymbol{d}_3(s) = \boldsymbol{m}\cdot(1+\kappa\tilde{t})\boldsymbol{g}^s = (1+\kappa\tilde{t})m^s$. Also,

$$\begin{aligned}\left(\frac{\partial m^t}{\partial \tilde{t}}\right)\boldsymbol{g}_t\boldsymbol{g}^t + \left(\frac{\partial m^t}{\partial s} - \kappa(1+\kappa t)m^s\right)\boldsymbol{g}_t\boldsymbol{g}^s &= \left(\frac{\partial m_{d_2}}{\partial s} - \kappa m_{d_3}\right)\frac{1}{(1+\kappa\tilde{t})}\boldsymbol{d}_2\otimes\boldsymbol{d}_3 \\ \left(\frac{\partial m^s}{\partial \tilde{t}} + \frac{\kappa}{(1+\kappa\tilde{t})}m^s\right)\boldsymbol{g}_s\boldsymbol{g}^t &= \left(\frac{\partial}{\partial \tilde{t}}\left(\frac{m_{d_3}}{(1+\kappa\tilde{t})}\right) + \frac{\kappa}{(1+\kappa\tilde{t})^2}m_{d_3}\right) \\ &\quad\times(1+\kappa\tilde{t})\boldsymbol{d}_3\otimes\boldsymbol{d}_2.\end{aligned} \tag{108}$$

Hence,

$$[\nabla\boldsymbol{m}]_{\boldsymbol{d}_i} = \begin{bmatrix} \frac{\partial m_{d_1}}{\partial \tilde{a}} & \frac{\partial m_{d_1}}{\partial \tilde{t}} & \frac{1}{(1+\kappa\tilde{t})}\frac{\partial m_{d_1}}{\partial s} \\ \frac{\partial m_{d_2}}{\partial \tilde{a}} & \frac{\partial m_{d_2}}{\partial \tilde{t}} & \frac{1}{(1+\kappa\tilde{t})}\left(\frac{\partial m_{d_2}}{\partial s} - \kappa m_{d_3}\right) \\ \frac{1}{(1+\kappa\tilde{t})}\frac{\partial m_{d_3}}{\partial \tilde{a}} & \frac{\partial m_{d_3}}{\partial \tilde{t}} & \frac{1}{(1+\kappa\tilde{t})}\left(\frac{\partial m_{d_3}}{\partial s} + \kappa m_{d_2}\right) \end{bmatrix}. \tag{109}$$

The exchange energy is thus expressed as

$$\mathcal{E}_{ex} = A\int_\Omega |\nabla\boldsymbol{m}|^2 d\tilde{t}d\tilde{a}ds. \tag{110}$$

Appendix C: Numerical Discretization of Equilibrium Equations

We demonstrate the discretization process for the equilibrium equation of a soft ferromagnetic ribbon under fixed-fixed boundary conditions (Eqn. (24)). We divide the domain into

$(N+2)$ nodal points, defined as $\bar{s}_i = ih$ for $i = 0, 1, \ldots, N+1$ where $h = \frac{1}{N+1}$. We utilize second-order accurate central difference scheme to approximate the second-order derivative in Eqn. (24). The discrete system of equations, along with the boundary conditions, is

$$\begin{gathered}\frac{\theta_{i-1} - 2\theta_i + \theta_{i+1}}{h^2} + \bar{P}\sin\theta_i + \bar{K}_d \sin 2\theta_i + \bar{R}\cos\theta_i = 0; \qquad i = 1, 2, \ldots, N, \\ \theta_0 = 0, \theta_{N+1} = 0,\end{gathered} \tag{111}$$

where θ_i denotes the numerical counterpart of $\theta(\bar{s} = \bar{s}_i)$.

Upon incorporating the boundary conditions, we assemble the discrete equations to form the following nonlinear system:

$$\underbrace{\frac{1}{h^2}\begin{bmatrix} -2 & 1 & 0 & & & & \\ 1 & -2 & 1 & & & & \\ 0 & \ddots & \ddots & \ddots & & & \\ & \ddots & 1 & -2 & 1 & \ddots & \\ & & & \ddots & \ddots & \ddots & \\ & & & & 1 & -2 & 1 \\ & & & & 0 & 1 & -2 \end{bmatrix}}_{\boldsymbol{K}} \underbrace{\begin{pmatrix} \theta_1 \\ \theta_2 \\ \vdots \\ \theta_i \\ \vdots \\ \theta_{N-1} \\ \theta_N \end{pmatrix}}_{\boldsymbol{\theta}} + \bar{P}\begin{pmatrix} \sin\theta_1 \\ \sin\theta_2 \\ \vdots \\ \sin\theta_i \\ \vdots \\ \sin\theta_{N-1} \\ \sin\theta_N \end{pmatrix} + \bar{K}_d \begin{pmatrix} \sin 2\theta_1 \\ \sin 2\theta_2 \\ \vdots \\ \sin 2\theta_i \\ \vdots \\ \sin 2\theta_{N-1} \\ \sin 2\theta_N \end{pmatrix} + \bar{R}\begin{pmatrix} \cos\theta_1 \\ \cos\theta_2 \\ \vdots \\ \cos\theta_i \\ \vdots \\ \cos\theta_{N-1} \\ \cos\theta_N \end{pmatrix} = \begin{pmatrix} 0 \\ 0 \\ \vdots \\ 0 \\ \vdots \\ 0 \\ 0 \end{pmatrix}. \tag{112}$$

In compact form, the discretized system can be written for all three cases (including the fixed-free case where $\bar{R} = 0$) as follows:

$$\boldsymbol{K\theta} + \bar{P}\sin\boldsymbol{\theta} + \bar{K}_d \sin 2\boldsymbol{\theta} + \bar{R}\cos\boldsymbol{\theta} = \boldsymbol{0}, \tag{113}$$

where $\boldsymbol{K}$ is the stiffness matrix and $\boldsymbol{\theta}$ is the vector containing the inclination angles at discrete points. It is noted that the matrix $\boldsymbol{K}$ is tridiagonal.

Upon discretizing the integral or isoperimetric constraint (Eqn. (25)) using the trapezoidal integration rule, we obtain:

$$\int_0^1 \sin\theta(\bar{s})d\bar{s} = 0 \implies \frac{h}{2}[\underbrace{\sin\theta_0}_{0} + 2(\sin\theta_1 + \cdots + \sin\theta_N) + \underbrace{\sin\theta_{N+1}}_{0}] = 0, \tag{114}$$

$$\implies \sin\theta_1 + \cdots + \sin\theta_N = 0. \tag{115}$$

This leads to the formation of a combined nonlinear set of equations:

$$\begin{pmatrix} \boldsymbol{K\theta} + \bar{P}\sin\boldsymbol{\theta} + \bar{K}_d \sin 2\boldsymbol{\theta} + \bar{R}\cos\boldsymbol{\theta} \\ \sin\theta_1 + \cdots + \sin\theta_N \end{pmatrix} = \begin{pmatrix} \mathbf{0} \\ 0 \end{pmatrix}, \tag{116}$$

$$\implies \boldsymbol{f}(\boldsymbol{\theta}, \bar{R}, \bar{P}) = \mathbf{0}. \tag{117}$$

Appendix D: Bifurcation Analysis

We briefly describe the bifurcation analysis for the planar deformation of ribbons, focusing on a specific case involving a soft ferromagnetic ribbon with fixed-fixed boundary conditions in the presence of an externally applied magnetic field $\boldsymbol{h}_e = h_e \boldsymbol{e}_2$. We begin by taking the second variation of the total magnetoelastic energy functional. Next, we perform a Fourier series expansion for kinematically-compatible variations. We then establish a stability criterion for the deformed configuration under various loading scenarios and end conditions. The numerical procedure to implement this stability criterion is explained in Sect. 5.

D.1 Derivation of Stability Condition

We determine the second variation of the functional $\delta^2\bar{\mathcal{E}}(\theta)$. To do this, we introduce a first-order perturbation in the assumed extremum θ. This perturbation is expressed as $\hat{\theta}(\bar{s}) = \theta(\bar{s}) + \epsilon\eta(\bar{s})$, where $\eta(\bar{s})$ is a kinematically admissible planar variation and ϵ is a positive scalar such that $\epsilon \ll 1$. Then, we substitute $\hat{\theta}(\bar{s})$ into Eqn. (21):

$$\begin{aligned} \bar{\mathcal{E}}(\theta + \epsilon\eta) = \int_0^1 \Bigg[& \frac{1}{2}\left(\theta'(\bar{s}) + \epsilon\eta'(\bar{s})\right)^2 + \bar{K}_d \cos^2(\theta(\bar{s}) + \epsilon\eta(\bar{s})) \\ & + \bar{P}\cos(\theta(\bar{s}) + \epsilon\eta(\bar{s})) - \bar{R}\sin(\theta(\bar{s}) + \epsilon\eta(\bar{s})) \Bigg] d\bar{s}. \end{aligned} \tag{118}$$

Differentiating the expression with respect to ϵ twice and then setting $\epsilon = 0$ yields the second variation of $\bar{\mathcal{E}}(\theta)$:

$$\begin{aligned} \delta^2\bar{\mathcal{E}}(\theta) &= \frac{\mathrm{d}^2}{\mathrm{d}\epsilon^2}\bar{\mathcal{E}}(\theta + \epsilon\eta)\Big|_{\epsilon=0} \\ &= \int_0^1 \eta'^2(\bar{s})d\bar{s} - 2\bar{K}_d \int_0^1 \cos 2\theta(\bar{s})\eta^2(\bar{s})d\bar{s} \\ &\quad - \bar{P}\int_0^1 \cos\theta(\bar{s})\eta^2(\bar{s})d\bar{s} + \bar{R}\int_0^1 \sin\theta(\bar{s})\eta^2(\bar{s})d\bar{s}. \end{aligned} \tag{119}$$

By integrating the first term by parts and applying the boundary conditions $\theta(0) = \theta(1) = \eta(0) = \eta(1) = 0$, we obtain:

$$\begin{aligned} \delta^2\bar{\mathcal{E}}(\theta) = \underbrace{\eta'(\bar{s})\eta(\bar{s})\Big|_0^1}_{=0} & - \int_0^1 \eta''(\bar{s})\eta(\bar{s})d\bar{s} - 2\bar{K}_d \int_0^1 \cos 2\theta(\bar{s})\eta^2(\bar{s})d\bar{s} \\ & - \bar{P}\int_0^1 \cos\theta(\bar{s})\eta^2(\bar{s})d\bar{s} + \bar{R}\int_0^1 \sin\theta(\bar{s})\eta^2(\bar{s})d\bar{s}, \end{aligned} \tag{120}$$

$$\implies \delta^2\bar{\mathcal{E}}(\theta) = -\int_0^1 \big[\eta''(\bar{s}) + 2\bar{K}_d\cos 2\theta(\bar{s})\eta(\bar{s}) + \bar{P}\cos\theta(\bar{s})\eta(\bar{s}) - \bar{R}\sin\theta(\bar{s})\eta(\bar{s})\big]\eta(\bar{s})d\bar{s}, \tag{121}$$

for all kinematically admissible functions $\eta(\bar{s})$. The stability criterion is:

$$\delta^2\bar{\mathcal{E}}(\theta)\begin{cases} > 0 & \text{stable} \\ < 0 & \text{unstable.} \end{cases} \tag{122}$$

The first variation to the integral constraint $\int_0^1 \sin\theta(\bar{s})d\bar{s} = 0$ is given by:

$$\int_0^1 \cos\theta(\bar{s})\eta(\bar{s})d\bar{s} = 0. \tag{123}$$

D.2 Construction of Sturm-Liouville Problem

A thorough investigation of the second variation $\delta^2\bar{\mathcal{E}}(\theta)$ requires the formulation of the following Sturm-Liouville problem, whose non-trivial solutions are denoted as $\phi_n(\bar{s})$:

$$\phi_n''(\bar{s}) + \lambda_n(2\bar{K}_d\cos 2\theta(\bar{s}) + \bar{P}\cos\theta(\bar{s}) - \bar{R}\sin\theta(\bar{s}))\phi_n(\bar{s}) = C_{R_n}\cos\theta(\bar{s}). \tag{124}$$

Here, λ_n are the eigenvalues and $\phi_n(\bar{s})$ are the corresponding eigenmodes of Eqn. (124). The function $L(\bar{s}) = (2\bar{K}_d\cos 2\theta(\bar{s}) + \bar{P}\cos\theta(\bar{s}) - \bar{R}\sin\theta(\bar{s}))$ represents the weight function. The term C_{R_n} enforces the isoperimetric constraint (Eqn. (123)). The conditions on $\phi_n(\bar{s})$ are:

- fixed-fixed case: $\phi_n(0) = \phi_n(1) = 0$ and $\int_0^1 \cos\theta(\bar{s})\phi_n(\bar{s})d\bar{s} = 0$,
- pinned-pinned case: $\phi_n'(0) = \phi_n'(1) = 0$ and $\int_0^1 \cos\theta(\bar{s})\phi_n(\bar{s})d\bar{s} = 0$,
- fixed-free case: $\phi_n(0) = \phi_n'(1) = 0$.

By multiplying both sides of Eqn. (124) by $\phi_n(\bar{s})$ and integrating over the domain, we can apply conditions imposed on $\phi_n(\bar{s})$. This procedure yields:

$$\int_0^1 [\phi_n''(\bar{s}) + \lambda_n L(\bar{s})\phi_n(\bar{s})]\phi_n(\bar{s})d\bar{s} = C_{R_n}\underbrace{\int_0^1 \cos\theta(\bar{s})\phi_n(\bar{s})d\bar{s}}_{0},$$

$$\implies \lambda_n\int_0^1 L(\bar{s})\phi_n^2(\bar{s})d\bar{s} = \int_0^1 \phi_n'^2(\bar{s})d\bar{s}. \tag{125}$$

We multiply Eqn. (124) by $\phi_m(\bar{s})$ and integrate over the domain to obtain:

$$\int_0^1 [\phi_n''(\bar{s}) + \lambda_n L(\bar{s})\phi_n(\bar{s})]\phi_m d\bar{s} = C_{R_n}\underbrace{\int_0^1 \cos\theta(\bar{s})\phi_m(\bar{s})d\bar{s}}_{0},$$

$$\implies -\int_0^1 \phi_n'(\bar{s})\phi_m'(\bar{s})d\bar{s} + \lambda_n\int_0^1 L(\bar{s})\phi_n(\bar{s})\phi_m(\bar{s})d\bar{s} = 0. \tag{126}$$

Similarly, consider Eqn. (64) for $\phi_m(\bar{s})$, multiply it by $\phi_n(\bar{s})$ and integrate by parts to obtain:

$$-\int_0^1 \phi_m'(\bar{s})\phi_n'(\bar{s})d\bar{s} + \lambda_m \int_0^1 L(\bar{s})\phi_n(\bar{s})\phi_m(\bar{s})d\bar{s} = 0. \tag{127}$$

Subtracting the second equation from the first yields:

$$(\lambda_n - \lambda_m)\int_0^1 L(\bar{s})\phi_n(\bar{s})\phi_m(\bar{s})d\bar{s} = 0. \tag{128}$$

For $n \neq m$, $\lambda_n \neq \lambda_m$, we obtain the orthogonality condition:

$$\int_0^1 L(\bar{s})\phi_n(\bar{s})\phi_m(\bar{s})d\bar{s} = 0. \tag{129}$$

Spectral Decomposition : We will employ $\phi_n(\bar{s})$ in conjunction with the weight function $L(\bar{s})$ to construct a Fourier series representation that converges in the mean to the square-integrable function $\eta(\bar{s})$:

$$\eta(\bar{s}) = \sum_{n=1}^{\infty} c_n \phi_n(\bar{s}), \qquad \text{where } c_n \text{ are Fourier coefficients.} \tag{130}$$

Substitute the above representation into Eqn. (121), we have:

$$\begin{aligned}
\delta^2\bar{\mathcal{E}}(\theta) &= -\int_0^1 [c_n\phi_n''(\bar{s}) + L(\bar{s})c_n\phi_n(\bar{s})]c_m\phi_m(\bar{s})d\bar{s} \\
&= -c_m c_n \int_0^1 [C_{R_n}\cos\theta(\bar{s}) - \lambda_n L(\bar{s})\phi_n(\bar{s})]\phi_m(\bar{s})d\bar{s} - c_n c_m \int_0^1 L(\bar{s})\phi_m(\bar{s})\phi_n(\bar{s})d\bar{s} \\
&= -c_m c_n C_{R_n} \underbrace{\int_0^1 \cos\theta(\bar{s})\phi_m(\bar{s})d\bar{s}}_{=0} + c_n c_m(\lambda_n - 1)\underbrace{\int_0^1 L(\bar{s})\phi_m(\bar{s})\phi_n(\bar{s})d\bar{s}}_{\text{(use orthogonality condition)}} \\
&= c_n^2(\lambda_n - 1)\int_0^1 L(\bar{s})\phi_n^2(\bar{s})d\bar{s} \\
&= c_n^2(\lambda_n - 1)\frac{1}{\lambda_n}\int_0^1 (\phi_n'(\bar{s}))^2 d\bar{s}.
\end{aligned}$$

Finally, we establish the stability criterion:

$$\implies \delta^2\bar{\mathcal{E}}(\theta) = \sum_{n=1}^{\infty} c_n^2\left(1 - \frac{1}{\lambda_n}\right)\int_0^1 (\phi_n'(\bar{s}))^2 d\bar{s} \quad \begin{cases} > 0 & \text{if } \lambda_n \notin [0,1] \quad \text{stable,} \\ < 0 & \text{if } \lambda_n \in [0,1] \quad \text{unstable.} \end{cases} \tag{131}$$

Acknowledgements We sincerely thank Professor R.D. James (University of Minnesota) for his valuable assistance in helping us understand the work of Moon and Pao and comparing it with our own. We would also like to acknowledge Professor Kaushik Bhattacharya (Caltech) for suggesting the calculations carried out in Sect. 6.4. We acknowledge Dr. Raghavendra Venkatraman (Courant Institute) for his valuable suggestions and insights on the draft of this paper. We also acknowledge Professor Ajeet Kumar (IIT, Delhi) for pointing out the validity of the Kirchhoff model. Furthermore, we would like to acknowledge the Indian Institute of Science Startup Grant and the Prime Minister's Research Fellowship (PMRF ID: 0201857) for providing financial support for this research.

Author contributions G. R. Krishna Chand Avatar: Data curation, Formal analysis, Investigation, Methodology, Resource, Software, Validation, Visualization, Writing – original draft, Writing – review & editing. V ivekanand Dabade: Conceptualization, Formal analysis, Funding acquisition, Investigation, Methodology, Project administration, Resources, Supervision, Validation, Writing – original draft, Writing – review & editing.

Data Availability No datasets were generated or analysed during the current study.

Declarations

Competing interests The authors declare no competing interests.

References

1. Audoly, B., Neukirch, S.: A one-dimensional model for elastic ribbons: a little stretching makes a big difference. J. Mech. Phys. Solids **153**, 104457 (2021). https://doi.org/10.1016/j.jmps.2021.104457
2. Bigoni, D., Bosi, F., Misseroni, D., Corso, F.D., Noselli, G.: New phenomena in nonlinear elastic structures: from tensile buckling to configurational forces. In: CISM International Centre for Mechanical Sciences, pp. 55–135. Springer, Vienna (2015). https://doi.org/10.1007/978-3-7091-1877-1_2
3. Brown, W.F.: Micromagnetics, vol. 18. Interscience, New York (1963)
4. Dabade, V., Venkatraman, R., James, R.D.: Micromagnetics of galfenol. J. Nonlinear Sci. **29**(2), 415–460 (2018). https://doi.org/10.1007/s00332-018-9492-8
5. Dabade, V., Venkatraman, R., James, R.D.: Micromagnetics of galfenol. J. Nonlinear Sci. **29**, 415–460 (2019)
6. Dacorogna, B.: Introduction to the Calculus of Variations, 3rd edn. World Scientific, Singapore (2014). https://books.google.co.in/books?id=QOU7DQAAQBAJ
7. Desimone, A., Kohn, R.V., Müller, S., Otto, F.: A reduced theory for thin-film micromagnetics. Commun. Pure Appl. Math. **55**(11), 1408–1460 (2002). https://doi.org/10.1002/cpa.3028
8. DeSimone, A., Kohn, R.V., Müller, S., Otto, F., et al.: Recent analytical developments in micromagnetics. Sci. Hysteresis **2**(4), 269–381 (2006)
9. Doedel, E., Keller, H.B., Kernevez, J.P.: Numerical analysis and control of bifurcation problems: (i) bifurcation in finite dimensions. Int. J. Bifurc. Chaos **01**(3), 493–520 (1991). https://doi.org/10.1142/s0218127491000397
10. Doedel, E., Keller, H.B., Kernevez, J.P.: Numerical analysis and control of bifurcation problems: (i) bifurcation in infinite dimensions. Int. J. Bifurc. Chaos **01**(4), 745–772 (1991). https://doi.org/10.1142/s0218127491000555
11. Gerbal, F., Wang, Y., Lyonnet, F., Bacri, J.C., Hocquet, T., Devaud, M.: A refined theory of magnetoelastic buckling matches experiments with ferromagnetic and superparamagnetic rods. Proc. Natl. Acad. Sci. USA **112**(23), 7135–7140 (2015). https://doi.org/10.1073/pnas.1422534112. https://www.pnas.org/doi/abs/10.1073/pnas.1422534112
12. Gioia, G., James, R.D.: Micromagnetics of very thin films. Proc. R. Soc. Lond., Ser. A, Math. Phys. Eng. Sci. **453**(1956), 213–223 (1997). https://doi.org/10.1098/rspa.1997.0013
13. James, R.: Configurational forces in magnetism with application to the dynamics of a small-scale ferromagnetic shape memory cantilever. Contin. Mech. Thermodyn. **14**(1), 55–86 (2002). https://doi.org/10.1007/s001610100072
14. Keip, M.A., Sridhar, A.: A variationally consistent phase-field approach for micro-magnetic domain evolution at finite deformations. J. Mech. Phys. Solids **125**, 805–824 (2019). https://doi.org/10.1016/j.jmps.2018.11.012
15. Levyakov, S.V., Kuznetsov, V.V.: Stability analysis of planar equilibrium configurations of elastic rods subjected to end loads. Acta Mech. **211**(1–2), 73–87 (2009). https://doi.org/10.1007/s00707-009-0213-0
16. Lum, G.Z., Ye, Z., Dong, X., Marvi, H., Erin, O., Hu, W., Sitti, M.: Shape-programmable magnetic soft matter. Proc. Natl. Acad. Sci. USA **113**(41), E6007–E6015 (2016)
17. Maddocks, J.H.: Stability of nonlinearly elastic rods. Arch. Ration. Mech. Anal. **85**(4), 311–354 (1984). https://doi.org/10.1007/BF00275737
18. Moon, F.: Magneto-Solid Mechanics. UMI Books on Demand. Wiley, New York (1984). https://books.google.co.in/books?id=RuxSAAAAMAAJ
19. Moon, F.C., Pao, Y.H.: Magnetoelastic buckling of a thin plate. J. Appl. Mech. **35**(1), 53–58 (1968). https://doi.org/10.1115/1.3601173

20. Peletan, L., Baguet, S., Torkhani, M., Jacquet-Richardet, G.: Quasi-periodic harmonic balance method for rubbing self-induced vibrations in rotor–stator dynamics. Nonlinear Dyn. **78**(4), 2501–2515 (2014). https://doi.org/10.1007/s11071-014-1606-8
21. Pressley, A.: Elementary Differential Geometry. Springer, London (2010). https://doi.org/10.1007/978-1-84882-891-9
22. Ramachandran, V., Bartlett, M.D., Wissman, J., Majidi, C.: Elastic instabilities of a ferroelastomer beam for soft reconfigurable electronics. Extrem. Mech. Lett. **9**, 282–290 (2016). https://doi.org/10.1016/j.eml.2016.08.007
23. Samourgkanidis, G., Kouzoudis, D.: Characterization of magnetoelastic ribbons as vibration sensors based on the measured natural frequencies of a cantilever beam. Sens. Actuators A, Phys. **301**, 111711 (2020)
24. Samy, O., Otsuji, T., El Moutaouakil, A.: Terahertz absorptance in mos2/graphene nanoribbon heterostructures. In: 2023 Photonics Electromagnetics Research Symposium (PIERS). IEEE (2023). https://doi.org/10.1109/PIERS59004.2023.10221462
25. Sheka, D.D., Pylypovskyi, O.V., Volkov, O.M., Yershov, K.V., Kravchuk, V.P., Makarov, D.: Fundamentals of curvilinear ferromagnetism: statics and dynamics of geometrically curved wires and narrow ribbons. Small **18**(12), 2105219 (2022)
26. Singh, R., Onck, P.: Magnetic field induced deformation and buckling of slender bodies. Int. J. Solids Struct. **143**, 29–58 (2018). https://doi.org/10.1016/j.ijsolstr.2018.02.029
27. Singh, K., Tipton, C.R., Han, E., Mullin, T.: Magneto-elastic buckling of an Euler beam. Proc. R. Soc. A, Math. Phys. Eng. Sci. **469**(2155), 20130111 (2013). https://doi.org/10.1098/rspa.2013.0111
28. Slastikov, V.V., Sonnenberg, C.: Reduced models for ferromagnetic nanowires. IMA J. Appl. Math. **77**(2), 220–235 (2011). https://doi.org/10.1093/imamat/hxr019
29. Streubel, R., Fischer, P., Kronast, F., Kravchuk, V.P., Sheka, D.D., Gaididei, Y., Schmidt, O.G., Makarov, D.: Magnetism in curved geometries. J. Phys. D, Appl. Phys. **49**(36), 363001 (2016)
30. Wang, L., Kim, Y., Guo, C.F., Zhao, X.: Hard-magnetic elastica. J. Mech. Phys. Solids **142**, 104045 (2020). https://doi.org/10.1016/j.jmps.2020.104045. https://www.sciencedirect.com/science/article/pii/S0022509620302805
31. Wang, L., Guo, C.F., Zhao, X.: Magnetic soft continuum robots with contact forces. Extrem. Mech. Lett. **51**, 101604 (2022). https://doi.org/10.1016/j.eml.2022.101604. https://www.sciencedirect.com/science/article/pii/S2352431622000013
32. Zhao, R., Kim, Y., Chester, S.A., Sharma, P., Zhao, X.: Mechanics of hard-magnetic soft materials. J. Mech. Phys. Solids **124**, 244–263 (2019). https://doi.org/10.1016/j.jmps.2018.10.008

Publisher's Note Springer Nature remains neutral with regard to jurisdictional claims in published maps and institutional affiliations.

Springer Nature or its licensor (e.g. a society or other partner) holds exclusive rights to this article under a publishing agreement with the author(s) or other rightsholder(s); author self-archiving of the accepted manuscript version of this article is solely governed by the terms of such publishing agreement and applicable law.